

Neural-network selection of high-redshift radio quasars, and the luminosity function at $z \sim 4$

D. Tuccillo,¹★ J. I. González-Serrano¹ and C. R. Benn²

¹*Instituto de Física de Cantabria (CSIC - Universidad de Cantabria), Av. de los Castros s/n, E-39005 Santander, Spain*

²*Isaac Newton Group, Apartado 321, E-38700 Santa Cruz de la Palma, Spain*

Accepted 2015 March 3. Received 2015 February 19; in original form 2014 July 18

ABSTRACT

We obtain a sample of 87 radio-loud quasi-stellar objects (QSOs) in the redshift range $3.6 \leq z \leq 4.4$ by cross-correlating sources in the Faint Images of the Radio Sky at Twenty-Centimeters (FIRST) radio survey ($S_{1.4\text{GHz}} > 1$ mJy) with star-like objects having $r < 20.2$ in Sloan Digital Sky Survey (SDSS) Data Release 7. Of these 87 QSOs, 80 are spectroscopically classified in previous work (mainly SDSS), and form the training set for a search for additional such sources. We apply our selection to 2916 FIRST-DR7 pairs and find 15 likely candidates. Seven of these are confirmed as high-redshift quasars, bringing the total to 87. The candidates were selected using a neural-network, which yields 97 per cent completeness (fraction of actual high- z QSOs selected as such) and an efficiency (fraction of candidates which are high- z QSOs) in the range of 47–60 per cent. We use this sample to estimate the binned optical luminosity function (LF) of radio-loud QSOs at $z \sim 4$, and also the LF of the *total* QSO population and its comoving density. Our results suggest that the radio-loud fraction at high z is similar to that at low z and that other authors may be underestimating the fraction at high z . Finally, we determine the slope of the optical LF and obtain results consistent with previous studies of radio-loud QSOs and of the whole population of QSOs. The evolution of the LF with redshift was for many years interpreted as a flattening of the bright-end slope, but has recently been re-interpreted as strong evolution of the break luminosity for high- z QSOs, and our results, for the radio-loud population, are consistent with this.

Key words: surveys – galaxies: active – galaxies: high-redshift – galaxies: luminosity function, mass function – quasars: general – cosmology: observations.

1 INTRODUCTION

Since their discovery in the 1960s (Hazard, Mackey & Shimmins 1963; Schmidt 1963), quasi-stellar objects (hereafter QSOs) have played a key role in extragalactic research, in particular in connection with studies of supermassive black holes (hereafter SMBHs), galaxy evolution, the intergalactic medium, large-scale structure and cosmology.

Quasar candidates are mainly identified from their optical colours in large sky surveys such as the 2dF survey (Boyle et al. 2000) and the Sloan Digital Sky Survey (SDSS; York et al. 2000; Schneider et al. 2010). Current data from SDSS provide us with photometric measurements for $\approx 5 \times 10^8$ galaxies, quasars and stars. The survey also provides spectra for nearly two million of these objects. This has dramatically increased the number of known QSOs, since the first edition of the SDSS quasar catalogue (Schneider et al. 2002). The fifth edition, which is based upon the SDSS Seventh Data Release (DR7), includes a remarkable 105 783 spectroscopically

confirmed QSOs (Schneider et al. 2010). Most of the SDSS QSO candidates were selected as spectroscopic targets on the basis of their non-stellar colours in *ugriz* bands and by matching unresolved sources to the FIRST radio survey (Faint Images of the Radio Sky at Twenty-Centimeters; Becker, White & Helfand 1995).

The SDSS QSO-selection algorithm was presented by Richards et al. (2002), and according to them is sensitive to QSOs at redshifts $z < \sim 5.8$. Completeness (fraction of QSOs selected as such) and efficiency (number of actual QSOs amongst the candidates divided by the total number of candidates) of the selection are a complex function of apparent magnitude i and redshift. Although QSOs of type 2 and certain QSOs of type 1 are missed, the overall estimated completeness is high (Vanden Berk et al. 2005), above 90 per cent for $16.0 \leq i \leq 19.0$ (Richards et al. 2006). At higher redshift, both completeness and efficiency drop, with an overall completeness of ~ 80 per cent for $3 \leq z \leq 5.3$ and efficiency ~ 55 per cent for QSOs with $z > 3$.

Determination of the QSO luminosity function (QLF) is important for the study of active galactic nuclei (hereafter AGN) and it requires QSO samples with a statistically significant number of sources and with accurately known completeness. In particular, an

★ E-mail: tuccillo@ifca.unican.es

accurate knowledge of the QLF at different epochs allows important constraints to be placed on the evolution of the mass function of SMBHs, on their growth and on the lifetime of the QSO phase (Volonteri, Haardt & Madau 2003; Netzer & Trakhtenbrot 2007; Shankar et al. 2010; Shen & Kelly 2012). The QLF also provides important information about the impact of QSO activity on the formation and evolution of the host galaxies (Cattaneo et al. 2009; Fabian 2012). In addition, it allows constraint of the contribution of AGN to the X-ray background (Ueda et al. 2003; Hickox & Markevitch 2006), the ultraviolet ionizing radiation (Samantaryay & Khare 2000; Giallongo et al. 2012) and the infrared background (Dole et al. 2006).

Radio-loud QSOs (hereafter RLQs) account for ~ 8 – 13 per cent of QSOs (Ivezić et al. 2002; Jiang et al. 2007; Baloković et al. 2012). The exact radio-loud fraction (RLF) is still unknown and it also depends on the definition of radio-loudness. Usually the latter is based on the radio luminosity P emitted by the source (e.g. Gregg et al. 1996, define an object to be radio-loud if $\log P_{1.4, \text{GHz}} (\text{W Hz}^{-1}) > 25.5$), or on R , the ratio between monochromatic radio and optical luminosities (Stocke et al. 1992). Some authors see no evidence for significant change of RLF with either redshift or luminosity (e.g. Goldschmidt et al. 1999; Stern et al. 2000; Cirasuolo et al. 2003; Vigotti et al. 2003), while others find that the RLF changes with both parameters (e.g. Miller, Peacock & Mead 1990; Schneider et al. 1992; Visnovsky et al. 1992; Jiang et al. 2007; Baloković et al. 2012). In particular Jiang et al. (2007), using a sample of 30 000 optically selected quasars from the SDSS quasar catalogue obtained from Data Release 3 (Schneider et al. 2005), find that the RLF of quasars decreases strongly with increasing redshift and decreasing luminosity.

Although only a small fraction of QSOs are radio-loud and, while they may not be fully representative of the entire population, they can be used to check the completeness of samples selected mainly on the basis of optical data, such as the SDSS QSO catalogues. For example, selection at radio wavelengths greatly reduces incompleteness due to the effects of dust obscuration, reddening and/or the presence of broad absorption lines (BALs; Carballo et al. 2008, hereafter C08, and McGreer, Helfand & White 2009). Selection in the radio is also more *efficient*, since it reduces stellar contamination.

In addition, increasing the number of known RLQ is important for understanding the origin of the radio phenomenon itself and for clarifying the connection between radio and optical activity in QSOs. Indeed, whether RLQ and radio-quiet QSOs are two physically distinct populations (the so-called radio-loudness dichotomy) or are part of a continuous sequence is still a matter of debate (see Jiang et al. 2007; Baloković et al. 2012; Kratzer 2014). As pointed out by several authors (e.g. Cirasuolo et al. 2003; Baloković et al. 2012), it would be helpful in the context of this debate, to have more homogeneous samples of QSOs, a larger number of QSOs with radio data available and a reduction of selection biases in flux-limited samples.

In this work, we present the results of a selection of RLQ with $3.6 \leq z \leq 4.4$. We start by cross-matching FIRST radio sources (from the 2003 April 11 release of the catalogue), with star-like objects in the SDSS DR7 photometric catalogue (Section 2). To select candidate high-redshift QSOs (Section 3), we use a simple but reliable neural-network (NN) algorithm already tested in previous work (Carballo et al. 2006; C08). Spectra of the resulting 15 candidates were obtained with the 2.5 m Nordic Optical Telescope (NOT) on La Palma (Spain) and these are presented in Section 4, together with checks of the completeness of our selection and com-

parisons of the completeness and efficiency with other work. In Section 5, we discuss the K -correction, and we present our sample of 87 $3.6 \leq z \leq 4.4$ RLQ. The various sources of incompleteness of this sample are discussed in Section 6. In Section 7, we calculate the optical luminosity function (LF) for $z \sim 3.8$ and 4.2 . In Section 8, we derive the space density of RLQ, and the space density of all QSOs, and discuss the LF. Our conclusions are summarized in Section 9.

All optical magnitudes are on the AB system. We use a Λ cold dark matter cosmology with $\Omega_\lambda = 0.7$, $\Omega_m = 0.3$ and $H_0 = 70 \text{ km s}^{-1} \text{ Mpc}^{-1}$.

2 DATA

2.1 Surveys used

In this work, we use the FIRST radio survey and the SDSS DR7 optical survey to obtain a radio-optical sample of QSO candidates in the redshift range $3.6 \leq z \leq 4.4$.

The FIRST survey was originally designed to produce the radio equivalent of the optical Palomar Observatory Sky Survey, using the National Radio Astronomy Observatory Very Large Array in its B-configuration at 1.4 GHz. Subsequently, the survey area was chosen to make it ideal for comparison with the SDSS. The survey produces images with 1.8 arcsec pixels, a resolution of 5 arcsec, a typical rms of 0.15 mJy and a flux-density limit of 1 mJy. The positional accuracy at the survey flux limit is ~ 1 arcsec. We used the 2003 April 11 version of the FIRST catalogue containing 811 117 sources covering a total area of 9033 deg^2 (8422 deg^2 in the Northern Galactic Cap and 611 deg^2 in the Southern Galactic Cap).

The SDSS DR7 (Abazajian et al. 2009) covers a total imaging area of $11\,663 \text{ deg}^2$ (7646 deg^2 in the Northern Galactic Cap). A total of 357 million distinct objects are included in the imaging catalogue, of which approximately 1.6 million are also included in the spectroscopic catalogue.

The survey reaches magnitude limits (95 per cent detection repeatability for point sources) in photometric bands u , g , r , i and z of 22.0, 22.2, 22.2, 21.3 and 20.5, respectively. Absolute astrometric errors are < 0.1 arcsec. In this paper, we consider only the images flagged by SDSS as ‘Primary’. These are unique detections, i.e. they do not include duplicate detections from the overlap between survey stripes. Each such object is associated with a run and a field which is the primary source of imaging data at this position.

To determine the overlap area of the two surveys, we first determined the area of the FIRST survey, which has an irregular boundary, by constructing a Delaunay triangulation using the source coordinates. We used code developed by Bernal (1988) which provides the coordinates of the vertices of the unique set of triangles over the FIRST area. We then computed the area covered by FIRST by adding up the areas of the individual triangles. The resulting area is 9032.27 deg^2 . Finally, for each FIRST source, we queried the SDSS data base to see if the position of the sources was included in the survey. The result of the query was that 89.38 per cent of FIRST sources fall in the SDSS-DR7 imaging area, implying an overlap of 8073.04 deg^2 .

2.2 Pre-selection criteria

We matched each FIRST source, not flagged as possible sidelobe or nearby bright source (~ 3.6 per cent of the sources in the catalogue have this warning flag), with the closest optical object in the ‘PhotoPrimary’ view of the SDSS DR7 catalogue within a 1.5 arcsec

radius. This radius is the same as used by C08, and is a compromise between completeness and efficiency. The adopted value is lower than the 2.0 arcsec radius used by SDSS in their algorithm for QSO selection. However, the excellent astrometry of FIRST and SDSS means that the peak in the distribution of optical/radio offsets occurs at about 0.2 arcsec (Schneider et al. 2010, Fig. 6), supporting our adoption of a 1.5 arcsec radius. From this match, we obtained a starting sample of 222 517 sources. In this sample, there is no selection by radio flux density or radio morphology other than the requirement that the radio source have at least a weak core component. The FIRST catalogue itself introduces several minor selection effects: the FIRST sensitivity limit is somewhat non-uniform over the sky, with small variations due to the observing strategy and large variations due to decreasing sensitivity in the vicinity of bright sources. However, the fraction of the survey area affected by sensitivity variations is small, less than 15 per cent (Becker et al. 1995). Another effect is that the FIRST survey limit of ≥ 1.0 mJy refers to the peak flux density of sources rather than to the integrated flux density; consequently, extended sources with total fluxes greater than 1 mJy may not appear in the catalogue because their peaks fall below the detection threshold.

From these 222 517 matches, we first selected the 13 956 star-like objects with $15.0 \leq r \leq 20.2$, where r refers to SDSS psfMag_r, corrected for Galactic extinction according to Schlegel, Finkbeiner & Davis (1998).

We then filtered the sample on the basis of several SDSS quality-control parameters used by others (e.g. Richards et al. 2002) when selecting QSO targets for spectroscopy. Specifically, we rejected all objects with magnitude errors > 0.2 mag in all five bands, and any for which the SDSS ‘fatal’ error flags ‘BRIGHT’, ‘SATURATED’, ‘EDGE’ or ‘BLENDED’ were set, indicating unreliable photometry. This left 13 287 objects.

Finally, in contrast with Richards et al. (2002), we rejected all objects with the ‘CHILD’ flag set (another 4148 sources), indicating objects obtained by deblending an image flagged ‘BLENDED’. This criterion ensures that only one optical object is associated with each radio source (Carballo et al. 2006), and we adopt it for consistency with C08. In this way, we avoid introducing differences in the pre-selection that may change the final efficiency of the NN algorithm. This is the main source of incompleteness in our sample, as will be discussed in Section 8.

This pre-selection process, summarized in Table 1, left us with 9139 star-like objects coinciding with FIRST radio sources.

3 SELECTION OF QSO CANDIDATES

3.1 NN algorithm

The machine-learning technique used in this work to select our list of QSO candidates is described in earlier papers (Carballo et al. 2006; C08), and here we give only a brief summary.

Table 1. Steps in the pre-selection process.

Pre-selection criterion	Selected sources
Starting FIRST-SDSS sample (≤ 1.5 arcsec)	222 517
$15 \leq r \leq 20.2$	74 853
Point-like	13 956
Without mag error > 0.2 in all bands	13 934
Exclude sources with ‘fatal’ error flags	13 287
Exclude sources with ‘CHILD’ flag	9139

We used a supervised artificial NN algorithm of feed-forward type, suitable for solving classification problems, and programmed using the MATLAB Neural Network Toolbox software. A supervised NN is trained with samples of known classification, in order to learn how to distinguish between the classes. Only after the training has been carried out, can the trained NN be used to classify a new problem sample. In our case, the classification task was formulated as a binary problem, the two classes being (a) the target class, i.e. QSOs in the redshift range $3.6 \leq z \leq 4.4$, and (b) the ‘non-target’ class, i.e. all other types of object.

In a feed-forward NN, each input variable corresponds to a node in the so-called ‘input layer’. Each of the input nodes has a weighted connection to every node in the next layer, called ‘the hidden layer’. A node in the hidden layer forms a weighted sum of its inputs, and then passes the information to a second hidden layer that performs a similar processing. The number of hidden layers, like the other parameters of the NN, has to be optimized for the problem that the NN aims to solve. The weighted information passes through the layers of the NN to the last ‘output’ layer, which performs a simple sum of its inputs, giving the output.

In particular, our NN was composed of the input layer, just one hidden layer, and an output layer y . The output y for the i th object, with values in the range (0, 1), is given by the non-linear function:

$$y^i = \frac{1}{1 + e^{-a^i}} \quad (1)$$

with $a^i = w_0 + \sum_{j=1}^d w_j x_j^i$, where $(x_1, x_2, \dots, x_d)^i$ are the input variables for object i . w_0 and (w_1, w_2, \dots, w_d) , called bias and weights, respectively, are the parameters fitted during the training. This NN model is known as *logistic linear discriminant*. The adopted error function was the variance of the outputs:

$$e = \frac{1}{m} \sum_{i=1}^m (y^i - T)^2, \quad (2)$$

where m is the number of objects used for the training and T is the target value, set to 1 for the class of high-redshift QSOs and 0 for the remaining sources, during the training. The optimal parameters for the net, i.e. those minimizing the error, were obtained using the Levenberg–Marquardt algorithm. This is a simple but robust function for optimization and it appears to be the fastest for the training of moderate-sized NNs (Hagan & Menhaj 1994).

The set of input variables adopted for the NN is the best set obtained in C08, i.e. a combination of optical magnitudes and colours ($r, u - g, g - r, r - i, i - z$) and radio-optical separation. The input variables were pre-processed, normalizing their values to the range $(-1, 1)$. No outliers required trimming. For this step, the whole pre-selected sample was used, regardless of whether the source was spectroscopically classified and thus suitable as a training object, or not. In fact, the input variables of the new objects (i.e. the problem objects) presented to the trained net are expected to be normalized in the same way as the ones used in the training process.

3.2 Spectroscopic classification of the pre-selected sample

Of the sample of 9139 sources passing initial selection (Table 1), 6091 have spectra in the SpecObj view of SDSS-DR7. 5348 of the latter are included in the fifth edition of the SDSS quasar catalogue (DR7 QSO catalogue; Schneider et al. 2010), which is also based on SDSS-DR7, but uses more stringent criteria for the classification of the objects as QSOs, in order to exclude dubious cases. 71 of the QSOs in this catalogue have redshifts in the range $3.6 \leq z \leq 4.4$.

The remaining 743 sources with spectra in DR7-SpecObj but not included in the DR7 QSO catalogue are classified by SDSS as stars, galaxies, quasars and sources of ‘unknown’ type. For all of these sources, a search was made in NED (the NASA/IPAC Extragalactic Database), and none of them was classified there as a $z \geq 3.6$ QSO. We also visually inspected the DR7-SpecObj spectra of these sources to check if any of them could be a QSO in the redshift range of interest here, but none of the objects, which include those with ‘unknown’ spectra, had spectral features consistent with a high- z QSO.

3048 of the 9139 sources in the sample lack spectroscopic classification in DR7-SpecObj. However, the DR7 QSO catalogue was compiled by inspecting all the SDSS spectra, not just those of the quasar candidates, and identified 115 of these as quasars (one of them being a high- z QSO in the redshift range of interest for our work) despite them not being automatically identified as such. Another 17 sources were identified as QSOs by C08, comprising 8 high- z QSOs and 9 QSOs with redshift below 3.6. The remaining 2916 sources were checked in NED, and none of them had been spectroscopically classified as of 2012 March.

A total of 6223 ($= 6091 + 115 + 17$) sources thus have a reliable spectroscopic classification. Of these, 80 ($= 71 + 1 + 8$) are QSOs in the redshift range $3.6 \leq z \leq 4.4$. These sources form the training sample, i.e. the sample used to train the NN to distinguish high- z QSOs in our redshift range of interest from other objects. Quasars with $3.6 \leq z \leq 4.4$ play the role of the target class. The non-target sources include stars, galaxies, QSOs with other redshifts and objects with spectra classed as ‘unknown’ but lacking the features expected for our target sources.

The 2916 sources without available spectra from SDSS-DR7 or from the literature (as of 2012 March) form the sample from which new QSO candidates in our redshift range of interest are selected using the trained NN.

3.3 Training and testing of the NN

Having defined the training sample, with 6223 spectroscopically classified sources, of which 80 are high-redshift QSOs, we are ready to train the NN and to test its performance as a classifier.

The classification algorithm fitted by the NN provides for each source an output $0 \leq y \leq 1$. The extreme values of 1 and 0 correspond, respectively, to sources with input variables more similar or less similar to those of the high- z QSO class. Objects with measured y greater than some threshold value y_c are candidate high- z QSOs.

The performance of the trained NN can be expressed in terms of two basic parameters: efficiency (or reliability) and completeness. In our case, the efficiency is the fraction of candidate high- z QSOs selected by the NN which are true high- z QSOs. The completeness is the fraction of true high- z QSOs with $y \geq y_c$, i.e. the fraction of true high- z QSOs selected as such by the NN.

The performance of the NN is ideally tested with a sample of objects not used during the training. In our case, since the target sample has only 80 objects, the ‘leave one out’ method was applied, using all but one of the objects for the training, and the remaining one for the test. In total, 6223 NNs were run, each of them providing the output for a test object. These output values, for a sample of 6223 test objects, were used to compute efficiency and completeness as a function of y_c , and the results are shown in Fig. 1. Since our purpose is to build a sample appropriate for statistical analysis, priority is given to completeness, accepting lower y values at the cost of lower efficiency. Choosing $y_c = 0.1$, our NN classifier has an efficiency

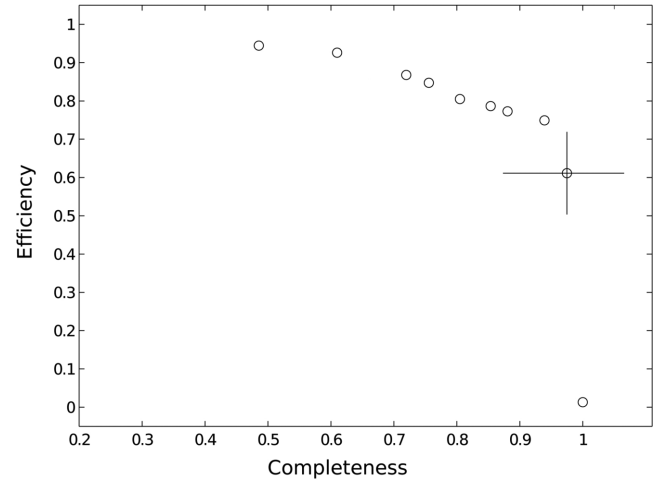


Figure 1. Efficiency versus completeness, measured for the test sample. Each symbol corresponds to a given value of the threshold y_c , ranging from 0.9 to 0, in increments of 0.1, from left to right. The symbol with the error bars correspond to the adopted threshold $y_c = 0.1$.

of 60 per cent ± 9 and a completeness of 97 per cent ± 11 (errors assume Poisson statistics).

3.4 High-redshift QSO candidates

The set of 6223 trained NNs used for the testing was applied to the sample of 2916 sources without spectra, in order to find candidate high- z QSOs. For each source, we adopted the median of the 6223 output values, and we selected as high-redshift QSO candidates those sources with $y_{\text{med}} > 0.1$. In this way, 15 QSO candidates in the range $3.6 \leq z \leq 4.4$ were found (Table 2), out of an original set of 2916 sources lacking spectroscopic identification.

4 CHECKS OF THE QSO SELECTION

Below we present spectroscopy of the 15 NN-selected high- z -QSO candidates (Section 4.1) and use SDSS DR9 to check the completeness of our selection (Section 4.2). In addition, we use our new data to assess the efficiency of high- z -QSO selection by C08 (Section 4.3) and to check the completeness of the spectroscopic identification of high- z QSOs in SDSS DR7 (Section 4.4).

4.1 Spectroscopy of the 15 NN-selected candidates

At the time, none of the 15 QSO candidates selected by our NN had spectra available in the literature. Therefore, long-slit spectra of all 15 were obtained with the 2.5-m NOT during the night of 2012 March 25, using ALFOSC (Andalucía Faint Object Spectrograph and Camera) with grism #4, which provides a dispersion of 3 Å per pixel. The spectral coverage was 4000–9000 Å and the resolution was 15 Å. The exposure time was about 1000 s per source, delivering signal-to-noise ratios $\gtrsim 8$ per pixel. The seeing was typically better than 1.3 arcsec FWHM. A spectrophotometric standard star was observed to correct for spectral response. After each target spectrum, an exposure of an arc lamp was

Table 2. Sample of 15 FIRST-SDSS DR7 high- z QSO candidates selected by our NN. The columns give the following: (1) SDSS J2000 coordinates; (2) SDSS dereddened PSF r magnitude; (3) FIRST peak radio flux density; (4) NN output; (5) QSO redshift determined in this work; (6) indicates if the source has a spectrum in SDSS-DR9; (7) indicates if the source was previously selected as a high- z candidate by C08; (8) BAL – broad-absorption-line QSO; LoBAL – low-ionization broad-absorption-line QSO.

RA (J2000) (1)	DEC (1)	r_{AB} (2)	$S_{1.4\text{GHz}}$ (mJy) (3)	y_{med} (4)	redshift (5)	DR9 (6)	C08 (7)	Notes (8)
08:15:55.02	+46:53:21.4	19.89	2.97	0.12	3.20		Yes	BAL
08:33:16.91	+29:22:28.0	20.13	12.63	0.32	3.30	Yes	Yes	
08:57:24.33	+11:05:49.2	19.81	1.91	0.98	3.71			
09:09:53.85	+47:49:43.2	19.90	373.29	0.22	3.64		Yes	
09:14:36.23	+50:38:48.5	20.19	47.98	0.15	3.62		Yes	
09:26:40.29	-02:30:41.5	19.82	1.9	0.12	3.76	Yes		
10:29:40.93	+10:04:10.9	19.47	2.81	0.22	3.40		Yes	
10:34:20.43	+41:49:37.5	20.12	2.17	0.30	4.00	Yes	Yes	
11:33:00.71	-04:11:58.5	19.96	9.64	0.12	3.39			BAL
11:51:07.42	+50:15:58.6	20.09	1.69	0.32	3.40		Yes	BAL
12:05:31.73	+29:01:49.2	20.17	1.51	0.50	3.44		Yes	BAL
12:13:29.43	-03:27:25.7	19.64	23.37	0.76	3.67		Yes	
12:28:19.97	+47:40:30.4	19.32	2.24	0.46	1.40		Yes	
12:44:43.07	+06:09:34.6	19.78	1.29	0.21	3.76	Yes	Yes	
15:43:36.59	+16:56:21.8	18.97	10.85	0.12	1.40			LoBAL

taken for wavelength calibration. Data were reduced using standard IRAF¹ routines.

All 15 candidates were confirmed as QSOs, 7 of them (Fig. 2) in the desired range of redshift, 5 in the nearby range $3.1 \leq z < 3.6$ (Fig. 3) and the remaining 3 at lower redshifts (Fig. 4). For the last three quasars at lower redshift, the NN misclassification is caused most likely by confusion of Mg II emission with Ly α emission. Table 2 lists the coordinates, r magnitudes, y_{med} values and redshifts for the 15 candidates. A note in column 6 indicates whether there is a spectrum of the object in the latest SDSS release DR9 (see the next subsection). We report also the discovery of five new BAL QSOs (see Table 2).

The observed efficiency of this selection is therefore ~ 47 per cent ($7 z > 3.6$ QSOs out of 15 candidates).

4.2 Check of completeness from SDSS DR9

As discussed in earlier sections, our methodology is applied to a sample of sources detected in both SDSS and FIRST using a match radius of 1.5 arcsec, and it makes use of photometric data in SDSS and of the radio-optical separation. Our pre-selection and selection methods are therefore based on the same variables as the SDSS target-selection algorithms. Therefore, we checked if the more recent SDSS-DR9 spectroscopic catalogue provides spectra of any of the 2916 sources lacking a spectral classification after SDSS-DR7 was released.

The ‘SpecObj’ view of SDSS-DR9 was used for this purpose, giving the following results. 4 of the 15 candidates have spectra in DR9 (see Table 2) with redshifts very similar to those reported in this work. Of the remaining 2901 sources rejected by the NN as high- z QSO candidates, 451 have

spectra in DR9 and 4 of them are classified as QSOs with $3.6 \leq z \leq 4.4$. However, examination of the spectra reveals that all four are actually lower redshift objects or stars. These objects are J075757.87+095607.56, J101403.75+451053.27, J112742.74+363429.5 and J222758.13+003705.45.

The fact that none of these 451 objects are classified in DR9 as high- z QSOs is consistent with the estimated high completeness of our NN algorithm: ~ 97 per cent. In Fig. 5 we report a schematic overview of the check discussed in this section.

4.3 Assessment of the sample of high- z candidates in C08

The selection of high- z QSOs in the present paper is based on more recent SDSS data releases than used by C08. However, the FIRST-SDSS pairs were obtained in this work in the same way as by C08, with similar criteria for the magnitude limits, the maximum radio-optical separation, optical morphology and photometric quality. Also the classification procedure, aimed at the identification of new high- z QSOs, uses similar NN architecture, input parameter-set, NN training and output parameter.

In C08, we used a training sample comprising 52 QSOs with $z \geq 3.6$, all from the DR5 spectroscopic catalogue, and selected 58 new candidates. In that paper, 24 of the candidates were confirmed as $z \geq 3.6$ QSOs (17 from observations obtained for the paper and 7 from the literature or from the DR6 spectroscopic catalogue). 16 sources were classified as other types of object, on the basis of observations by C08, or spectra from the literature or DR6. 18 high- z QSO candidates remained unclassified at C08.

11 of the 18 C08 candidates overlap with the 15 candidate-QSOs identified in this work. As result of our observations, these 11 sources were classified as 5 high- z QSOs, 5 QSOs with $3.2 \leq z \leq 3.5$ and a QSO at $z = 1.40$ (see Table 2). The remaining seven candidates of C08 consist of three QSOs included in the DR7 QSO catalogue and in our training sample (SDSS 110946.44+190257.6 with $z = 3.67$, SDSS 123128.22+184714.3 with $z = 3.33$ and SDSS

¹ IRAF is distributed by the National Optical Astronomy Observatories, which is operated by Association of Universities for Research in Astronomy, Inc., under cooperative agreement with the National Science Foundation.

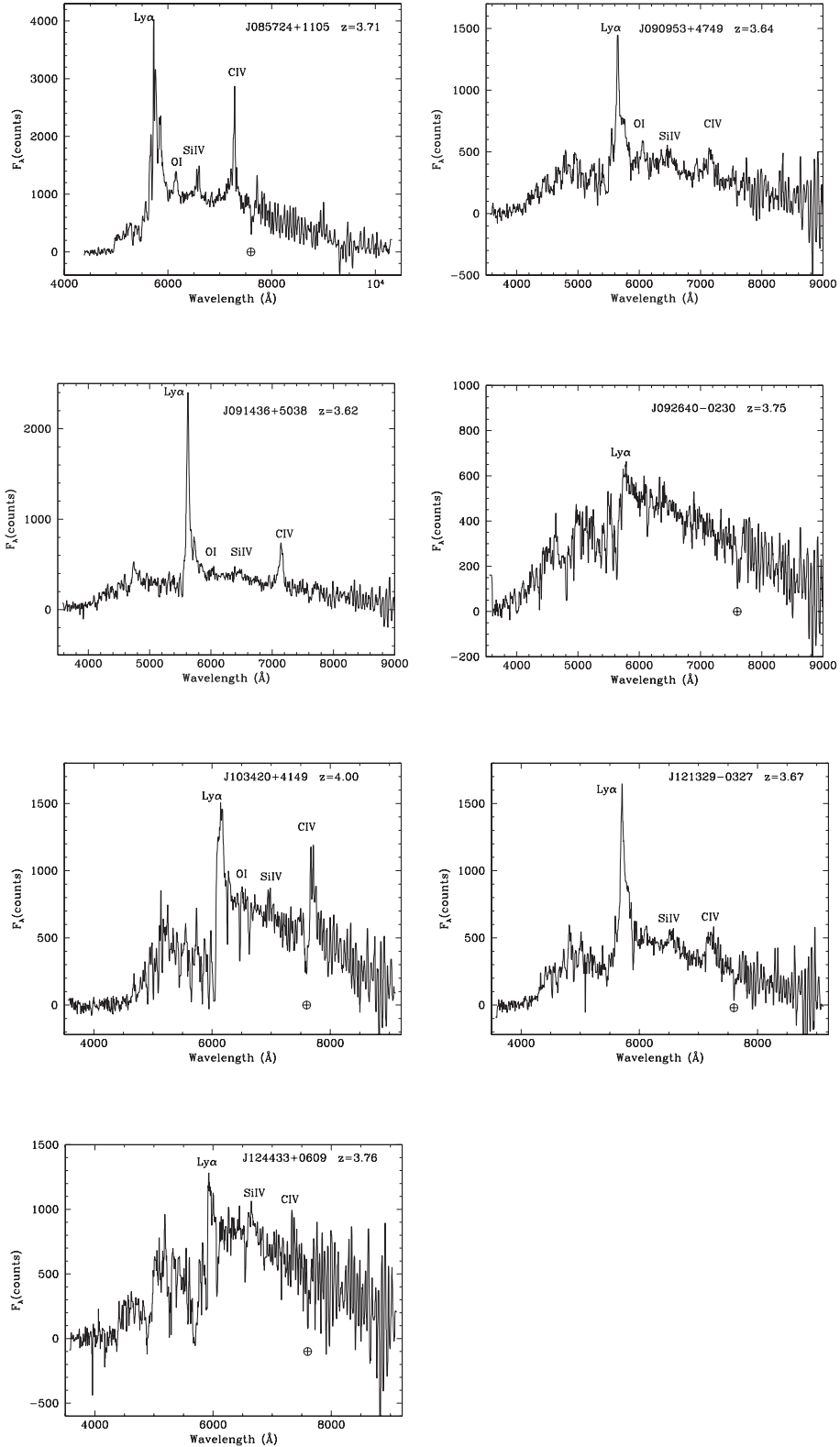


Figure 2. NOT/ALFOSC spectra of NN-selected high- z candidates: QSOs with $3.6 \leq z \leq 4.4$.

124323.16+235842.2 with $z = 3.49$) and four sources not selected by our classifier as being high- z QSOs. The spectra of three of these four sources were obtained in our observing programme at the NOT, yielding QSOs at $z = 3.44$ and 1.4 and a late-type star (see Table 3, and Figs 3 and 4 for spectra).

The spectroscopic observations of the 58 high- z candidates at C08 are now almost complete (57 out of 58). They yield an efficiency of 52 ± 9 per cent (30/58), highlighting the value of simple NN for this classification task. This efficiency is in reasonable agreement with the value obtained with the training sample, i.e. with the expectation

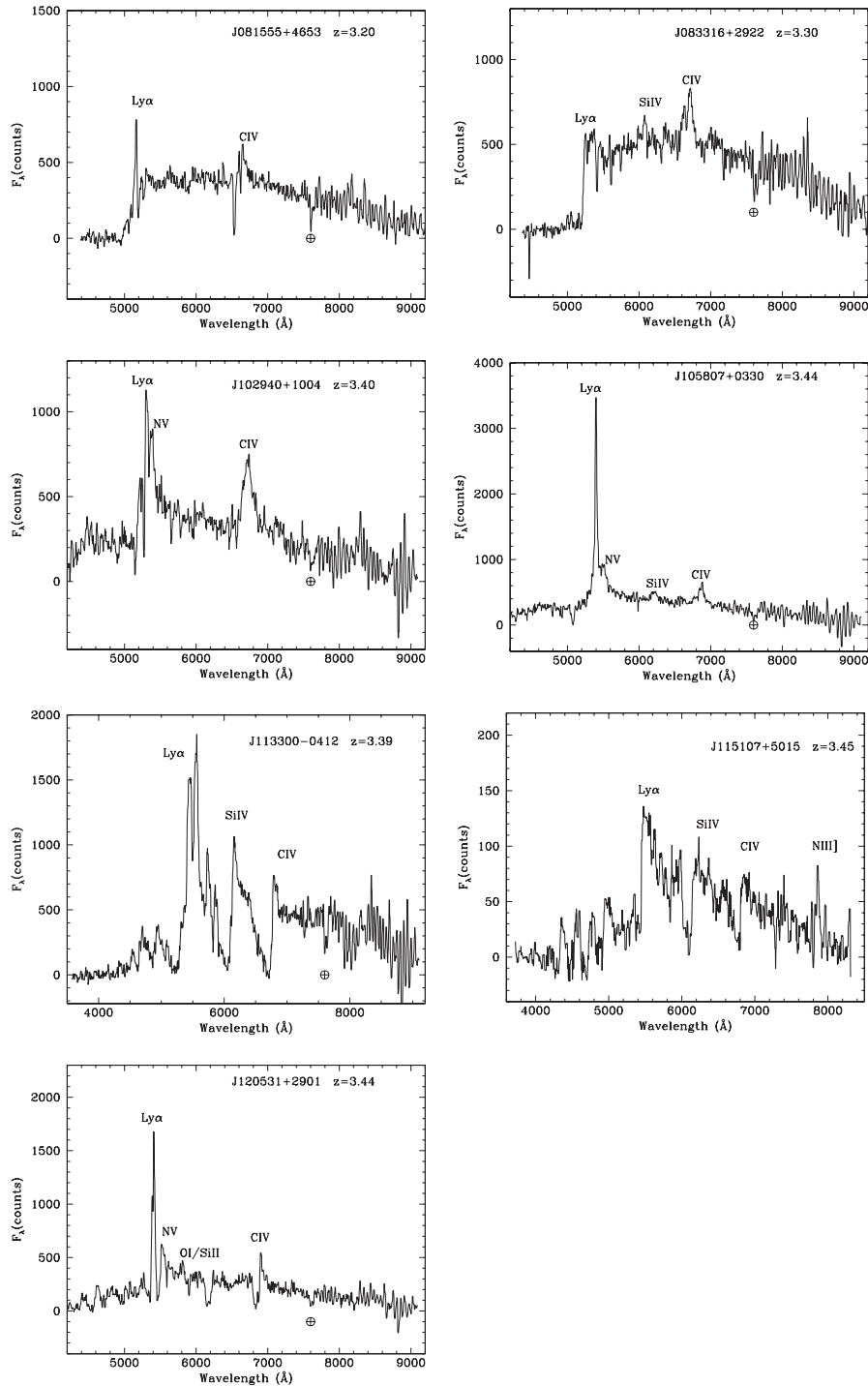


Figure 3. NOT/ALFOSC spectra of NN-selected high- z candidates: QSOs with $3.0 \leq z < 3.6$.

we had from the objects with known classification, 62 ± 9 per cent (C08). In addition, we note that a large fraction of the contaminants, 15 out of 28, are QSOs with $3.1 \leq z < 3.6$, close to the redshift threshold we adopted.

4.4 Spectroscopic completeness of SDSS for high- z QSOs

Several studies of the SDSS selection of QSOs (Richards et al. 2002, 2006; Croom et al. 2004; McGreer et al. 2009) suggest an overall completeness above 90 per cent. The completeness in gen-

eral decreases with increasing redshift and decreasing brightness, and it is particularly inefficient for $2.2 < z < 3$ where quasar and star colours are very similar. In particular, McGreer et al. (2009) studied the completeness of quasar selection at redshift $z > 3.5$ and magnitude $i < 20.2$, and found for the SDSS target algorithm a completeness of ≈ 86 per cent, in good agreement with the 85 per cent derived in Richards et al. (2006).

The analysis in this paper and in C08 identifies 15 QSOs with $3.6 \leq z \leq 4.4$, missed by SDSS-DR7 (two have spectra in SDSS-DR9, which uses BOSS). This allows us to estimate the

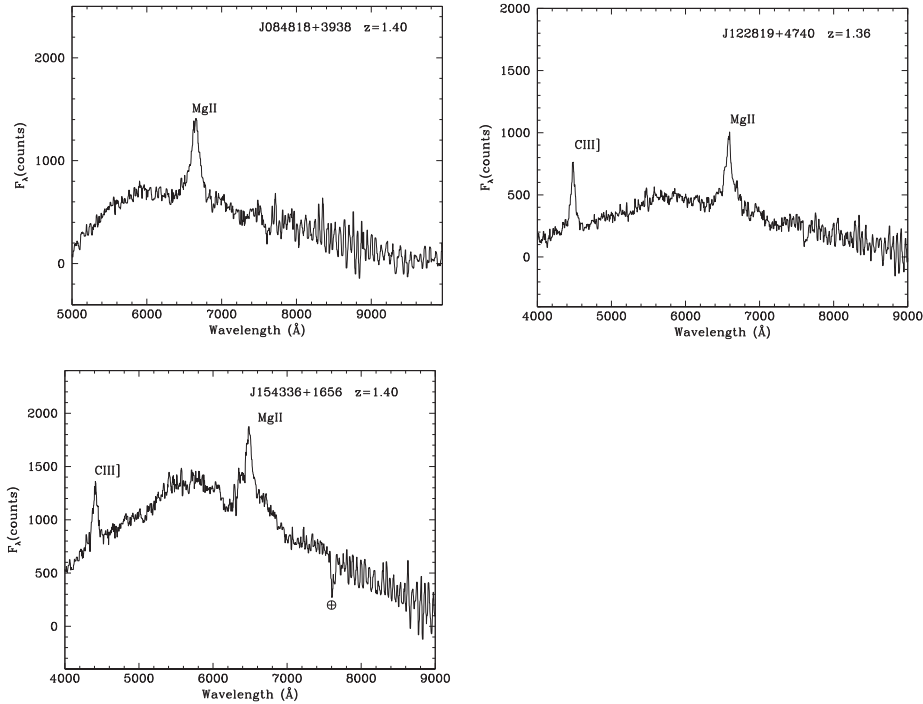


Figure 4. NOT/ALFOSC spectra of NN-selected high- z candidates: QSOs with $z < 3$.

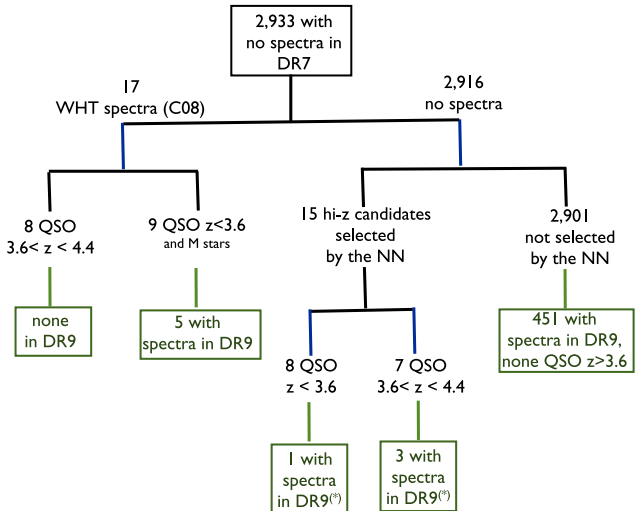


Figure 5. Schematic overview of a check of the efficiency of our selection via comparison with DR9 spectroscopic information. See Section 4.2. The 2916 objects (Section 3.2) without spectra in DR7, or in the literature, were classified by our NN, with 15 being selected by the NN as high-redshift candidates. (*) = targets from BOSS (Baryon Oscillations Spectroscopic Survey).

incompleteness of the SDSS-DR7 selection, after allowing for the fact that the spectroscopic area of the SDSS survey is ~ 95 per cent of the imaging area. 4 of our 15 QSOs $3.6 \leq z \leq 4.4$ lie outside the SDSS spectroscopic plates, so the estimated incompleteness in SDSS is 11 QSOs out of 83 (87 minus 4) in this redshift range, i.e. ~ 13 per cent ± 4 , in good agreement with estimates by McGreer et al. (2009) and Richards et al. (2002).

In Fig. 6, we plot the $g - i$, $r - z$ colour–colour diagram of the entire training sample together with the 15 $3.6 \leq z \leq 4.4$ QSOs

Table 3. Spectra of three high- z QSO candidates from C08, not selected by our NN, but observed to complete the C08 sample. The columns give the following: (1) SDSS J2000 coordinates; (2) SDSS dereddened PSF r magnitude; (3) FIRST peak radio flux density; (4) QSO redshift or spectral classification; (5) indicates if the source has a spectrum in SDSS-DR9.

RA (J2000) (1)	DEC (J2000) (2)	r_{AB} (3)	$S_{1.4\text{GHz}}$ (mJy) (4)	Redshift (5)	DR9 (6)
08:48:18.88	+39:38:06.0	20.15	1.28	1.4	
10:58:07.47	+03:30:59.6	19.91	4.18	3.44	Yes
12:04:07.84	+48:45:48.0	19.97	3.96	M-star	

missed by SDSS and identified by us. Splitting the sample between QSOs with $3.6 \leq z \leq 4.4$ and all other sources, we note that our QSO-selection method is sensitive even at the boundary of the two samples, demonstrating the effectiveness of learning-machine techniques, when compared with simple colour-cut criteria.

5 FINAL SAMPLE

In Table 4, we present the final sample of 87 QSOs with $3.6 \leq z \leq 4.4$ satisfying our selection criteria. This sample includes 72 QSOs (see Section 3.2) from the fifth quasar catalogue (Schneider et al. 2010) plus 15 QSOs revealed by our NN (8 from C08 and 7 from this work, see Section 4.1). The magnitude limit for our sample is $r_{AB} = 20.2$. To convert to absolute magnitudes M_r , a K -correction (Humason, Mayall & Sandage 1956) is required.

Following the convention of Hogg et al. (2002), the K -correction between a bandpass R used to observe a source at redshift z and the same bandpass in the rest frame, is

$$m_R = M_R + D_M(z) + K_R(z), \quad (3)$$

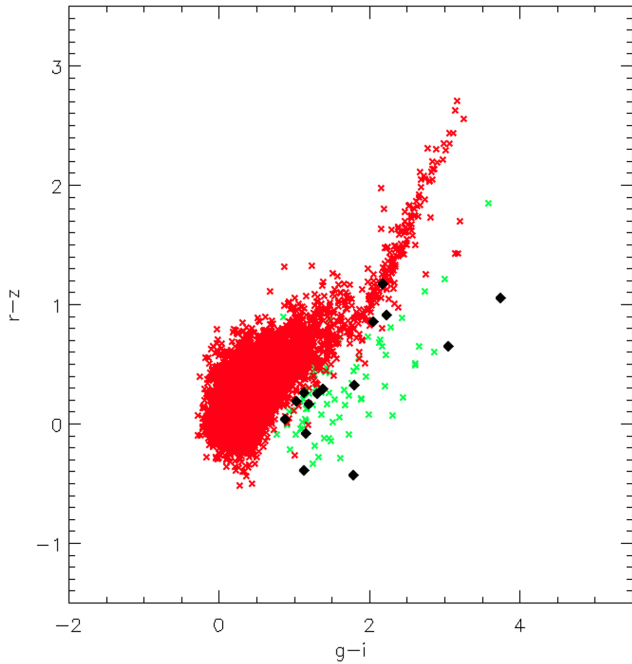


Figure 6. Colour–colour diagram of the 6233 sources with spectra in DR7, with green crosses representing QSOs with $3.6 \leq z \leq 4.4$, and red crosses representing other objects. The new 15 QSOs with $3.6 \leq z \leq 4.4$ (8 from C08, 7 from this work, all missed by SDSS) are plotted as black diamonds.

where $D_M(z)$ is the distance modulus calculated from the luminosity distance D_L as $D_M = 5 \log_{10} \left(\frac{D_L}{10 \text{ pc}} \right)$, m_R is the apparent magnitude, and M_R is the absolute magnitude.

An accurate K -correction, including the contribution of emission lines, can be computed by convolving a typical QSO spectrum at different redshifts with the filter response (e.g. Cristiani & Vio 1990; Wisotzki 2000, the latter based on optical/UV spectra from Elvis et al. 1994). Following this approach, we calculated the K -correction by convolving the Vanden Berk et al. (2001) composite quasar spectrum with the SDSS r -filter:

$$K = 2.5 \log_{10} \left[(1+z) \frac{\int_0^\infty F(\lambda) S(\lambda) d\lambda}{\int_0^\infty F((\lambda)/(1+z)) S(\lambda) d\lambda} \right], \quad (4)$$

where $F(\lambda)$ is the measured intensity per unit wavelength, and $S(\lambda)$ is the r -band filter response. The resulting K -correction is shown in Fig. 7 and in Table 5.

To convert from M_r to the commonly used monochromatic absolute AB magnitude at 1450 \AA , M_{1450} , we assume the canonical power-law spectral energy distribution with spectral index $\alpha_\nu = -0.5$ and hence

$$M_{1450} = M_r + 2.5 \alpha_\nu \log_{10} \left(\frac{1450 \text{ \AA}}{6231 \text{ \AA}} \right) = M_r + 0.791, \quad (5)$$

where 6231 \AA is the effective wavelength of the SDSS r filter. We use this spectral index rather than that derived by Vanden Berk et al. (2001, $\alpha_\nu = -0.44$) to allow a direct comparison with other authors. We also avoid using the composite spectrum in Vanden Berk et al. (2001) to convert from 6231 to 1450 \AA rest-frame flux density since above $H\beta$ there is a significant contribution from stellar light from low-redshift quasar hosts, which we effectively eliminate by extrapolating the power law to red wavelengths.

6 COMPLETENESS

Below we estimate the completeness (number of QSOs selected divided by the actual number of QSOs in this range of redshift) of the sample of 87 RLQ with $3.6 \leq z \leq 4.4$. This sample will be used (in Section 7) to calculate the LF. There are several sources of incompleteness: exclusion of optical images of poor quality (Section 6.1); radio-survey incompleteness and missed radio-optical identifications (Section 6.2); and incompleteness of selection by the NN algorithm (Section 6.3).

6.1 Optical image quality

Due to the sensitivity of our NN to data of poor photometric quality, we discarded at the pre-selection stage (Section 2.2) objects having ‘fatal’ error flags or magnitude errors larger than 0.2 in all five bands (Richards et al. 2002) or flagged CHILD.

Incompleteness due to the exclusion of fatal and non-fatal photometric errors (Richards et al. 2002 define as ‘non-fatal’ errors: some empirical combination of SDSS flags generally associated with poor deblends of complex objects) during the SDSS selection of QSO-candidates was discussed by Richards et al. (2006) who applied a global 5 per cent correction. In previous evaluations of this selection effect, Croom et al. (2004) suggest 6 per cent incompleteness for objects with $17.5 \leq i \leq 18.5$, and Vanden Berk et al. (2005) estimated an incompleteness of 3.8 per cent for point-like objects with $i < 19.1$.

To quantify the incompleteness of our selection due to the exclusion of CHILD objects, we evaluated the fraction of such objects amongst $15 \leq r \leq 20.2$ QSOs in the fifth SDSS quasar catalogue, which did not exclude CHILD objects. The fraction that we derive in this way is 27 per cent. The net completeness due to exclusion of these two types of object is therefore 69 per cent (0.95×0.73).

These fractions are in approximate agreement with the statistics of Table 1, which indicate 4.8 per cent incompleteness due to ‘fatal’ errors (669 rejected out of a total of 13 956 sources), and 31 per cent incompleteness due to the exclusion of sources flagged as CHILD (4148 out of 13 287), i.e. a net completeness of 66 per cent (0.95×0.69).

For the analysis here, we adopt an intermediate estimated completeness of 68 per cent.

We do not apply any correction for objects misclassified in SDSS as having galaxy morphology but being star-like objects. Tests of random samples of sources with available spectra indicate that this source of incompleteness is < 0.03 per cent.

6.2 Radio incompleteness

Two sources of incompleteness arise from radio selection using the FIRST survey.

6.2.1 Incompleteness of FIRST survey

The completeness of the FIRST survey as a function of flux density has been estimated for SDSS quasars and is given in fig. 1 of Jiang et al. (2007, and is discussed elsewhere, e.g. by Prandoni et al. 2001). At integrated FIRST flux density $> 3 \text{ mJy}$, FIRST is > 96 per cent complete and the completeness declines with decreasing flux density. From the results of these studies, we assume the following

Table 4. Final sample of 87 RLQ with $3.6 \leq z \leq 4.4$ (continued on the next page). The columns give the following: (1) SDSS object-ID (2) SDSS J2000 coordinates; (3) SDSS dereddened PSF r magnitude; (4) error in PSF r magnitude as given in SDSS; (5) QSO redshift determined in this work or from SDSS; (6) FIRST peak radio flux density; (7) absolute r magnitude; (8) radio luminosity at 1.4 GHz; (9) indicates the source of the data from which the redshift was first obtained (the two WHT sources are from Benn et al. 2002).

NAME	RA	DEC	r_{AB}	σ_r	Redshift	$S_{1.4\text{GHz}}$	M_r	$\log_{10} P_{1.4\text{GHz}}$	ID
(1)	(J2000)	(J2000)	(3)	(4)	(5)	(mJy)	(7)	(W Hz ⁻¹)	(9)
J015339.61-001104.9	01:53:39.61	-00:11:05.0	18.83	0.022	4.19	4.82	-28.59	26.42	SDSS
J030025.23+003224.2	03:00:25.23	+00:32:24.2	19.68	0.025	4.18	7.75	-27.74	26.62	SDSS
J072518.26+370518.3	07:25:18.27	+37:05:18.4	19.60	0.020	4.33	26.72	-27.94	27.19	WHT
J074711.14+273903.3	07:47:11.15	+27:39:03.4	18.35	0.025	4.15	1.08	-29.04	25.76	SDSS
J074738.49+133747.3	07:47:38.49	+13:37:47.3	19.35	0.015	4.17	7.18	-28.05	26.59	WHT
J075113.04+312038.0	07:51:13.05	+31:20:38.0	19.73	0.020	3.76	5.84	-27.29	26.42	SDSS
J075122.35+452334.2	07:51:22.36	+45:23:34.2	20.20	0.033	3.61	1.18	-26.73	25.69	SDSS
J080710.74+131739.4	08:07:10.74	+13:17:39.4	20.00	0.026	3.73	48.20	-27.00	27.32	SDSS
J081009.95+384757.0	08:10:09.95	+38:47:57.1	19.62	0.018	3.94	26.68	-27.57	27.11	SDSS
J082323.32+155206.8	08:23:23.32	+15:52:06.8	19.30	0.018	3.78	74.93	-27.74	27.53	SDSS
J083322.50+095941.2	08:33:22.50	+09:59:41.2	18.69	0.016	3.73	122.52	-28.31	27.73	SDSS
J083808.46+534809.8	08:38:08.46	+53:48:09.9	19.94	0.032	3.61	8.47	-27.00	26.54	SDSS
J083946.22+511202.8	08:39:46.22	+51:12:02.9	19.31	0.016	4.39	40.50	-28.28	27.38	SDSS
J084044.19+341101.6	08:40:44.19	+34:11:01.6	19.78	0.020	3.89	13.64	-27.35	26.81	SDSS
J085257.12+243103.1	08:52:57.12	+24:31:03.2	19.46	0.016	3.62	157.30	-27.48	27.81	SDSS
J085501.81+182437.7	08:55:01.82	+18:24:37.7	19.96	0.020	3.96	9.38	-27.25	26.66	SDSS
J085724.32+110549.1	08:57:24.33	+11:05:49.2	19.81	0.017	3.71	1.91	-27.17	25.92	NOT
J085944.06+212511.1	08:59:44.06	+21:25:11.2	18.74	0.015	3.70	23.54	-28.24	27.01	SDSS
J090254.16+413506.5	09:02:54.17	+41:35:06.5	20.12	0.023	3.69	1.12	-26.85	25.68	WHT
J090953.85+474943.2	09:09:53.85	+47:49:43.2	19.90	0.020	3.64	373.29	-27.05	28.19	NOT
J091436.23+503848.5	09:14:36.23	+50:38:48.5	20.19	0.028	3.62	47.98	-26.75	27.30	NOT
J091824.38+063653.3	09:18:24.38	+06:36:53.4	19.76	0.022	4.19	25.87	-27.66	27.15	SDSS
J092640.28-023041.4	09:26:40.29	-02:30:41.5	19.82	0.021	3.76	1.90	-27.20	25.93	NOT
J092832.87+184824.3	09:28:32.88	+18:48:24.4	17.54	0.016	3.77	8.67	-29.49	26.59	SDSS
J093714.48+082858.5	09:37:14.49	+08:28:58.5	18.58	0.015	3.70	3.47	-28.40	26.18	SDSS
J094003.03+511602.7	09:40:03.03	+51:16:02.7	19.00	0.014	3.60	12.90	-27.94	26.72	SDSS
J100012.26+102151.8	10:00:12.26	+10:21:51.9	19.54	0.023	3.64	21.87	-27.41	26.96	SDSS
J101747.75+342737.8	10:17:47.76	+34:27:37.9	20.00	0.031	3.69	2.83	-26.98	26.08	SDSS
J103055.95+432037.7	10:30:55.95	+43:20:37.7	19.84	0.025	3.70	31.29	-27.14	27.13	SDSS
J103420.43+414937.5	10:34:20.43	+41:49:37.5	20.12	0.029	4.00	2.17	-27.12	26.03	NOT
J103446.54+110214.4	10:34:46.54	+11:02:14.5	18.81	0.025	4.27	1.15	-28.68	25.81	SDSS
J103717.72+182303.0	10:37:17.72	+18:23:03.1	19.81	0.023	4.05	13.59	-27.48	26.84	SDSS
J105121.36+612038.0	10:51:21.37	+61:20:38.1	18.92	0.020	3.69	6.90	-28.06	26.47	SDSS
J105756.25+455553.0	10:57:56.26	+45:55:53.1	17.45	0.022	4.14	1.10	-29.93	25.77	SDSS
J110147.88+001039.4	11:01:47.89	+00:10:39.4	20.18	0.026	3.69	192.10	-26.79	27.92	SDSS
J110543.86+255343.1	11:05:43.87	+25:53:43.1	20.09	0.026	3.75	1.69	-26.92	25.87	SDSS
J110946.44+190257.6	11:09:46.44	+19:02:57.6	20.05	0.024	3.67	7.22	-26.91	26.49	SDSS
J111055.21+430510.0	11:10:55.22	+43:05:10.1	18.58	0.024	3.82	1.21	-28.50	25.74	SDSS
J111701.89+131115.4	11:17:01.90	+13:11:15.4	18.28	0.018	3.62	28.00	-28.66	27.07	SDSS
J111736.33+445655.6	11:17:36.33	+44:56:55.7	20.05	0.026	3.85	24.33	-27.05	27.05	SDSS
J112339.59+291710.7	11:23:39.60	+29:17:10.8	19.46	0.017	3.77	3.68	-27.57	26.22	SDSS
J112530.49+575722.7	11:25:30.50	+57:57:22.7	19.43	0.036	3.68	2.52	-27.54	26.03	SDSS
J112749.45+051140.5	11:27:49.45	+05:11:40.6	19.14	0.012	3.71	2.34	-27.84	26.01	SDSS
J112938.73+131232.2	11:29:38.73	+13:12:32.3	18.78	0.026	3.61	1.77	-28.16	25.86	SDSS
J113330.91+380638.1	11:33:30.91	+38:06:38.2	19.71	0.025	3.63	1.39	-27.23	25.76	SDSS
J113729.42+375224.2	11:37:29.43	+37:52:24.2	20.18	0.032	4.17	2.70	-27.22	26.16	SDSS
J115045.61+424001.1	11:50:45.61	+42:40:01.1	19.88	0.019	3.87	1.82	-27.23	25.93	SDSS
J115449.36+180204.3	11:54:49.36	+18:02:04.4	19.61	0.024	3.69	37.99	-27.36	27.21	SDSS
J120447.15+330938.7	12:04:47.15	+33:09:38.8	19.23	0.025	3.62	1.10	-27.71	25.66	SDSS
J121329.42-032725.7	12:13:29.43	-03:27:25.7	19.64	0.027	3.67	23.37	-27.33	27.00	NOT
J122027.95+261903.5	12:20:27.96	+26:19:03.6	18.13	0.017	3.70	34.34	-28.85	27.17	SDSS
J123142.17+381658.9	12:31:42.17	+38:16:58.9	20.18	0.030	4.14	20.44	-27.19	27.03	SDSS
J124054.91+543652.2	12:40:54.91	+54:36:52.2	19.74	0.023	3.94	14.89	-27.44	26.86	SDSS
J124209.81+372005.6	12:42:09.81	+37:20:05.6	19.34	0.018	3.84	644.79	-27.75	28.47	SDSS
J124443.06+060934.6	12:44:43.07	+06:09:34.6	19.78	0.024	3.76	1.29	-27.24	25.76	NOT
J124658.82+120854.7	12:46:58.83	+12:08:54.7	20.01	0.024	3.80	1.07	-27.05	25.69	SDSS
J124943.67+152707.0	12:49:43.67	+15:27:07.1	19.34	0.019	3.99	1.75	-27.90	25.94	SDSS

Table 4 – continued

NAME	RA	DEC	r_{AB}	σ_r	Redshift	$S_{1.4\text{GHz}}$	M_r	$\log_{10} P_{1.4\text{GHz}}$	ID
(1)	(2)	(J2000)	(3)	(4)	(5)	(mJy)	(7)	(W Hz ⁻¹)	(9)
J130348.94+002010.5	13:03:48.94	+00:20:10.5	18.89	0.019	3.65	1.08	-28.06	25.66	SDSS
J130738.83+150752.0	13:07:38.83	+15:07:52.1	19.72	0.027	4.11	3.44	-27.63	26.26	SDSS
J131242.86+084105.0	13:12:42.86	+08:41:05.0	18.52	0.014	3.74	4.41	-28.49	26.29	SDSS
J131536.57+485629.0	13:15:36.58	+48:56:29.1	19.76	0.025	3.62	9.94	-27.18	26.61	SDSS
J132512.49+112329.7	13:25:12.49	+11:23:29.8	19.32	0.022	4.41	69.39	-28.28	27.61	SDSS
J134854.37+171149.6	13:48:54.37	+17:11:49.6	19.13	0.021	3.62	2.10	-27.81	25.94	SDSS
J135406.89-020603.2	13:54:06.90	-02:06:03.2	19.17	0.018	3.72	709.05	-27.82	28.49	SDSS
J135554.56+450421.0	13:55:54.56	+45:04:21.1	19.36	0.021	4.09	1.48	-27.98	25.89	SDSS
J140635.66+622543.3	14:06:35.67	+62:25:43.4	19.73	0.020	3.89	11.03	-27.41	26.72	WHT
J140850.91+020522.7	14:08:50.91	+02:05:22.7	19.08	0.017	4.01	1.47	-28.17	25.87	SDSS
J142209.70+465932.5	14:22:09.70	+46:59:32.5	19.72	0.022	3.81	10.56	-27.35	26.68	SDSS
J142326.48+391226.2	14:23:26.48	+39:12:26.3	20.15	0.024	3.92	6.63	-27.01	26.50	SDSS
J143413.05+162852.7	14:34:13.06	+16:28:52.7	19.86	0.022	4.19	4.90	-27.56	26.42	SDSS
J143533.78+543559.2	14:35:33.78	+54:35:59.2	20.04	0.025	3.81	93.26	-27.02	27.63	SDSS
J144542.76+490248.9	14:45:42.76	+49:02:48.9	17.32	0.009	3.87	2.51	-29.80	26.07	SDSS
J144643.36+602714.3	14:46:43.37	+60:27:14.4	19.79	0.033	3.78	1.87	-27.25	25.92	SDSS
J145329.01+481724.9	14:53:29.01	+48:17:24.9	20.12	0.030	3.77	4.42	-26.91	26.30	WHT
J150328.88+041949.0	15:03:28.89	+04:19:49.0	17.96	0.017	3.66	122.70	-29.00	27.72	SDSS
J150643.80+533134.4	15:06:43.81	+53:31:34.5	18.94	0.022	3.79	13.97	-28.11	26.80	SDSS
J151146.99+252424.3	15:11:46.99	+25:24:24.3	19.95	0.024	3.72	1.24	-27.04	25.73	SDSS
J152028.14+183556.1	15:20:28.14	+18:35:56.2	19.82	0.021	4.12	6.26	-27.54	26.52	SDSS
J153336.13+054356.5	15:33:36.14	+05:43:56.5	19.84	0.020	3.94	27.55	-27.34	27.13	SDSS
J161716.49+250208.1	16:17:16.49	+25:02:08.2	19.98	0.023	3.94	1.01	-27.20	25.69	SDSS
J161933.65+302115.0	16:19:33.65	+30:21:15.1	19.53	0.025	3.81	3.88	-27.53	26.25	SDSS
J163708.29+091424.5	16:37:08.30	+09:14:24.6	19.57	0.018	3.75	9.51	-27.45	26.62	WHT
J163950.52+434003.6	16:39:50.52	+43:40:03.7	17.95	0.017	3.99	23.78	-29.28	27.07	SDSS
J164326.24+410343.4	16:43:26.24	+41:03:43.4	20.10	0.025	3.87	63.40	-27.02	27.47	SDSS
J222814.40-085525.7	22:28:14.40	-08:55:25.7	20.18	0.034	3.64	1.99	-26.77	25.92	WHT
J223535.59+003602.0	22:35:35.59	+00:36:02.1	20.15	0.027	3.87	5.06	-26.97	26.38	NOT
J235022.40-095144.3	23:50:22.40	-09:51:44.4	19.67	0.021	3.70	6.37	-27.31	26.44	WHT

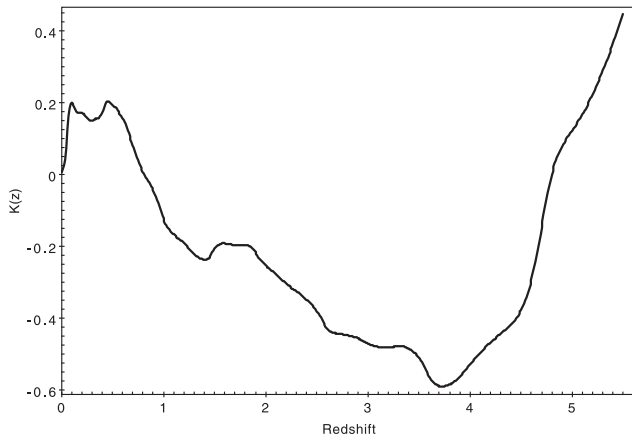


Figure 7. Computed K -correction in r . A tabulation is available online, and a sample is shown in Table 5.

completeness function, $q(S)$, where S is the FIRST integrated flux density in mJy:

$$q(S) = \begin{cases} 0.50, & S \leq 1.25 \\ 0.75, & 1.25 < S \leq 2 \\ 0.85, & 2 < S \leq 3 \\ 0.95, & 3 < S \leq 5 \\ 1, & S > 5. \end{cases} \quad (6)$$

In Fig. 8, we show for our sample the cumulative distribution of integrated radio flux densities, for objects fainter than 10 mJy.

Applying $q(S)$ to our final sample, we obtain a completeness of 84 per cent (87 QSOs detected and ~ 16 missed), for the flux-density limit of 1 mJy.

Table 5. K -correction in the SDSS r band (Fig. 7). A portion of the table is shown here. The full table is available online.

z_{em}	K correction
0.01	0.0075
0.02	0.0151
0.03	0.0241
0.04	0.0412
0.05	0.0720
0.06	0.1236
0.07	0.1619
0.08	0.1851
0.09	0.1959
0.10	0.1999
0.11	0.1985
0.12	0.1939

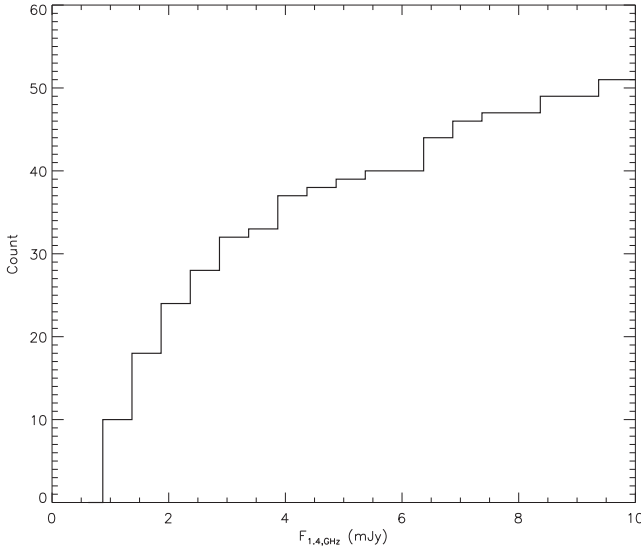


Figure 8. Cumulative distribution of FIRST flux densities for those QSOs in our sample of 87 with $3.6 \leq z \leq 4.4$, and with radio flux density < 10 mJy.

6.2.2 Match radius

To obtain our radio-optical sample, we sought simple one-to-one matches within radius 1.5 arcsec. We used this criterion for consistency with C08, who adopted this on the basis that more than 99 per cent of FIRST-APM (Automatic Plate Measuring Facility catalog of POSS I) QSOs with $3.8 \leq z \leq 4.5$, $E \leq 18.8$ and $S_{1.4\text{GHz}} > 1$ mJy fall within this radius (Vigotti et al. 2003).

However, a simple one-to-one match between FIRST and SDSS will miss double-lobe QSOs without detected radio cores. De Vries, Becker & White (2006) found that for a sample of 5515 FIRST-SDSS QSOs with radio morphological information within 450 arcsec, the fraction of FIRST-SDSS double-lobe QSOs with undetected cores is 3.7 per cent. Since the starting samples of SDSS QSOs in de Vries et al. (2006) and in this work obey similar SDSS selection criteria, we used this value to correct for this source of incompleteness.

6.3 Incompleteness of selection by the NN

The completeness of our NN classifier was estimated as 97 per cent, from the testing on known high- z QSOs presented in Section 3.3. The classifier selected 15 high- z QSO candidates and rejected 2901. Of the later, 451 have now spectroscopy from DR9 and none of them was identified as a high- z QSO, confirming this high level of completeness (see Section 4.2).

6.4 Net completeness

The net completeness of our sample of 87 RLQ at $3.6 \leq z \leq 4.4$ (Section 5) is the product of each of the completeness terms discussed above: acceptance of only those candidates with high-quality photometry (Section 6.1, 68 per cent completeness); completeness of the FIRST radio survey (Section 6.2.1, 84 per cent for our sample); acceptance of only optical-radio matches within a given radius and exclusion of extended sources (Section 6.2.2, 99 and 96.3 per cent); and the completeness of the NN-selection algorithm (Section 6.3, 97 per cent).

Multiplying these four terms together, the net completeness for our sample is 53 per cent.

7 BINNED LF

7.1 Method

Using the final sample of 87 QSOs listed in Section 5 and correcting for incompleteness as discussed in Section 6, we compute the binned QLF in the redshift range $3.6 \leq z \leq 4.4$.

The binned QLF is usually calculated using the classical $1/V_{\text{max}}$ method (Schmidt 1968; Maccacaro et al. 1991; Ellis et al. 1996), or its generalized version (usually known as $\sum V_a^{-1}$) applied to samples comprising subsamples with different flux limits (Avni & Bahcall 1980).

The V_{max} method is an unbiased (Felten 1976) non-parametric estimator of the space density. It is commonly used to fit models of the LF, since it has the advantage that it does not assume any underlying model. Even when the model LF is fitted to the unbinned data (for example in the maximum-likelihood technique of Marshall et al. 1983), it is often used before performing the fit to observe the overall behaviour of the LF.

However Page & Carrera (2000) demonstrated that the $\sum 1/V_{\text{max}}$ estimator introduces significant errors for objects close to the flux limits of the survey. An alternative method proposed by Page & Carrera (2000) is superior and partially corrects for this source of error, although implicitly assumes a uniform distribution of the sources within each bin (Miyaji, Hasinger & Schmidt 2001; Croom et al. 2009). The variation of the LF within a bin can be particularly critical at the steep bright end of the QSO LF. Instead, we used a modified version of the Page & Carrera (2000) method that does not make use of the uniform-distribution assumption and is still model independent.

To illustrate the method used in this paper, we start with a brief overview of the $1/V_{\text{max}}$ and the Page & Carrera (2000) methods. The LF is defined as the number of objects per unit of comoving volume, per unit of luminosity. A naive approach to the calculation of space density in an interval $[L_1, L_2] \times [V_1(z_1), V_2(z_2)]$ of luminosity and redshift, centred upon values L^* and z^* , would be to simply count the number of objects N within the interval considered:

$$\Phi(L^*, z^*) = \frac{N}{\Delta V \Delta L}. \quad (7)$$

The $1/V_{\text{max}}$ method, first proposed by Schmidt (1968), takes into account the fact that in flux-limited samples there is a higher probability to observe a bright source than a faint one. Thus, the count of sources N is replaced with a sum of probabilities:

$$\sum_1^N \frac{V_0}{V_{\text{max},i}}, \quad (8)$$

where V_0 is the volume over which we are computing the LF, and $V_{\text{max},i}$ is the maximum volume at which the source could be observed and still be included in our sample. In this way, the computation of the LF becomes

$$\Phi(L, z) = \frac{1}{\Delta L} \sum_1^N \frac{1}{\Delta V_{\text{max},i}}. \quad (9)$$

Page & Carrera (2000) noted that the limit in apparent magnitude of the survey bounds the region of integration. In particular, for a given bin in redshift, L_1 and L_2 should be replaced by the actual luminosity limits (L_{min} , L_{max}) as determined by the intersections

with the limiting-magnitude curves of the survey. Therefore, $\Phi(L, z)$ is calculated as

$$\Phi(L, z) = \frac{N}{\int_{L_{\min}}^{L_{\max}} \int_{z_{\min}}^{z_{\max}(L)} (dV/dz) dz dL}, \quad (10)$$

where z_{\min} is the bottom of the redshift interval and $z_{\max}(L)$ is the highest possible redshift for an object of luminosity L within the considered bin Δz . This approach takes into account the real area of integration but implicitly assumes uniform distribution of sources over the bin.

In order to minimize this bias, we calculate the maximum actual integration area determined as in Page & Carrera (2000) but for each source in the bin, so as not to lose the V_{\max} information for individual sources. Then, we sum over all the sources in the bin. In this way, we do not count the number of sources over an area larger than that of the actual survey and at same time, within a single bin, we weight sources by luminosity. Finally, $\Phi(L, z)$ is calculated as

$$\Phi(L, z) = \sum_{i=1}^N \frac{1}{\int_{L_{\min}}^{L_{\max,i}} \int_{z_{\min}}^{z_{\max}(L,i)} (dV/dz) dz dL}. \quad (11)$$

The difference between this methodology and that of Page & Carrera (2000) is negligible in the case of a large sample of QSOs uniformly distributed in (M, z) space, but becomes critical for small samples not distributed uniformly in each bin, as is the case here. In Fig. 9, we show the volume–luminosity space available to an object in a bin intersected by a limiting-magnitude curve, (a) in the Page & Carrera (2000) approach, (b) in the classical $1/V_{\max}$ case and (c) for the methodology used here.

The statistical uncertainty $\delta\Phi$ is calculated for each bin i as

$$\delta\Phi_i = \frac{\Phi_i}{\delta N_0}. \quad (12)$$

Where N_0 is the actual number of objects in the bin and $\delta N_0 = \sqrt{N_0}$ (Poisson statistics). The formula is easily derived, when the space density Φ_i is assumed to be approximately:

$$\Phi_i \approx \frac{N}{V_e L_e} = \frac{N_0 f}{V_e L_e}, \quad (13)$$

where $(V_e L_e)$ is an equivalent space–luminosity area, and N is the corrected number of quasars in bin i . The error in the completeness factor f is assumed to be ≈ 0 .

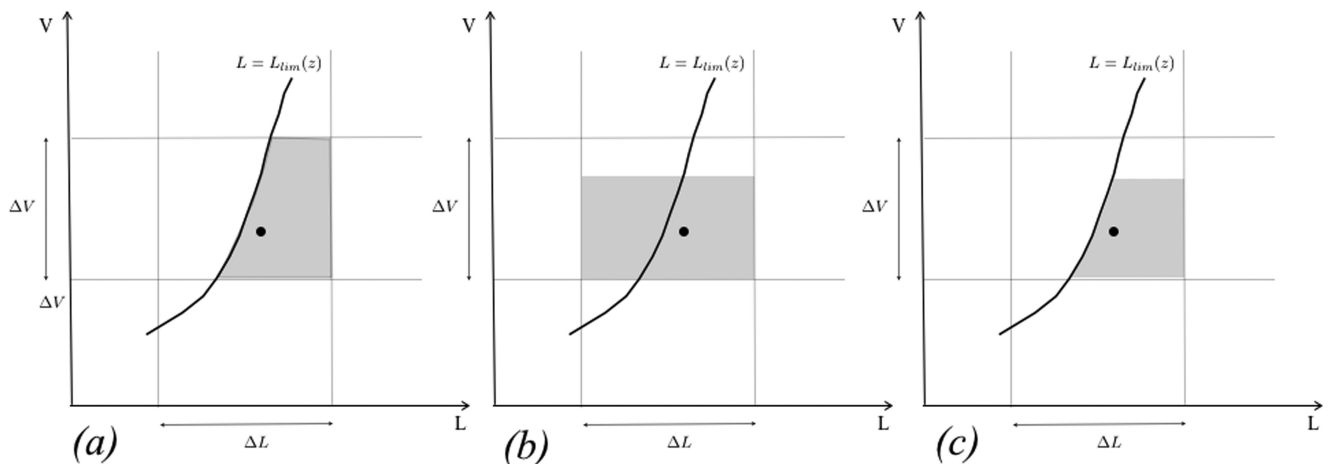


Figure 9. Volume–luminosity space used to calculate the contribution to the LF from a single object (the black dot) in a given bin intersected by the line $L = L_{\lim}(z)$, i.e. the minimum detectable luminosity of an object at redshift z . The available space (grey shaded area) is shown for a binned LF calculated using (a) the Page & Carrera implementation, (b) the classical $1/V_{\max}$ method and (c) our methodology.

7.2 The QLF

The QLF was computed using two bins in redshift, 3.6–4.015 and 4.015–4.415, and 11 bins in optical absolute magnitude starting with $M_r = -26.6$ and with $\Delta M = 0.3$. In Fig. 10, we plot M_r versus redshift for our sample of QSOs; the dotted grid shows the bins in magnitude and redshift used to compute the QLF. The curves show the upper and lower limiting apparent magnitude r of our selection. The top and side panels show the marginal distributions in redshift and absolute magnitude, respectively.

Since our complete sample results from two surveys with different flux limits, the maximum redshift at which a source can be observed may be different in the two surveys. The most efficient way to combine areas with different flux limits is to assume that each object could be found in any of the survey areas for which it is brighter than the corresponding flux limit. This is ‘coherent’ addition of samples, in the language of Avni & Bahcall (1980). Therefore, since our survey is a radio-optical survey, for each source we chose the smaller of $z_{\max, \text{optical}}$ and $z_{\max, \text{radio}}$.

For each bin, we applied the completeness corrections as explained in Section 6 and computed the weighted number of QSOs in the bin. Table 6 and Fig. 11 show the resulting QLF for RLQ. In Fig. 11, we plot separately the LF for the two bins of redshift, at $z \sim 3.8$ and 4.2. We also show the best-fitting slopes which will be discussed in Section 8.3.

8 DISCUSSION

Below we use the binned LF calculated from the previous section to derive the space density of RLQ at $3.6 \leq z \leq 4.4$ (Section 9.1). We then derive the space density of the entire population (i.e. radio-loud + radio-quiet) of QSOs at this redshift (Section 8.2) using two independent estimates of the RLF (Sections 8.2.1, 8.2.2). Finally, we derive the slope of the LF of RLQ at $z \sim 3.8$ and at $z \sim 4.2$, and compare our results with those of other authors (Section 8.3).

Our sample includes QSOs with optical luminosities $M_r < -26.6 \Leftrightarrow M_{1450} \lesssim -25.8$ (see equation 3). We adopt the definition of radio-loudness used by Gregg et al. (1996), i.e. $\log P_{1.4, \text{GHz}} > 25.5$. All the sources included in our sample (i.e. $S_{1.4 \text{GHz}} > 1 \text{ mJy}$) meet this criterion and are therefore radio-loud. Due to the limit in flux density, the minimum radio luminosity

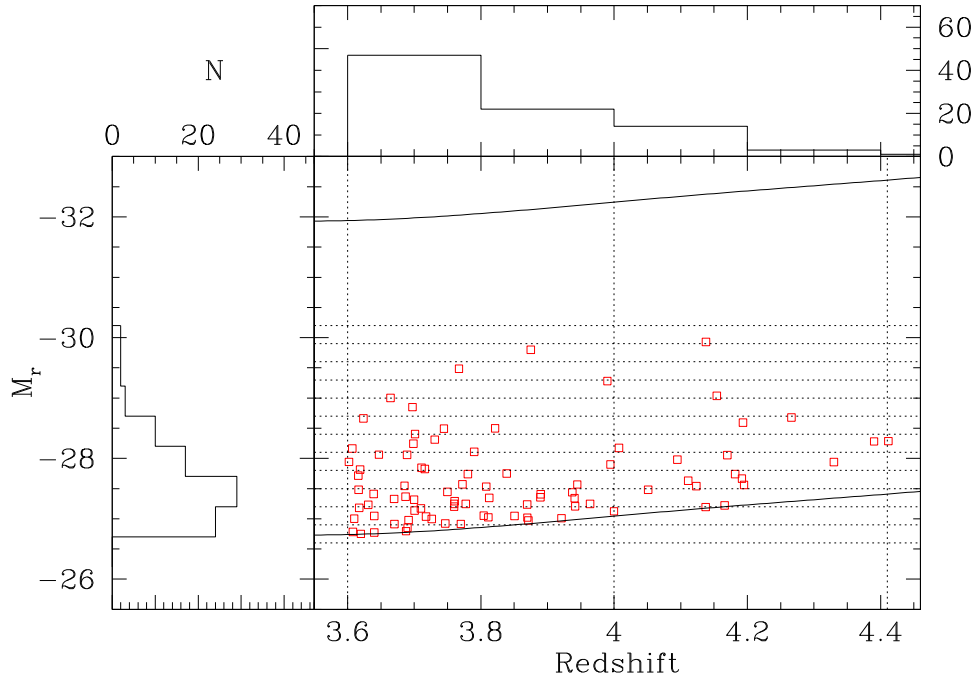


Figure 10. Luminosity-redshift diagram for the complete sample of 87 RLQ. The dotted lines show the limits of the bins ($\Delta L \Delta z$) used to compute the LF. Solid lines represent the upper ($r = 15$) and lower ($r = 20.2$) limits of the survey. Upper and left-hand panels show marginal histograms of redshift and absolute magnitude, respectively (see Section 7.2).

Table 6. Binned LF for FIRST-SDSS quasars at redshift ~ 4 . The columns give the following: (1) median redshift of the bin, (2) median absolute magnitude M_r of the bin, (3) space density ϕ_{RL} ($\text{Mpc}^{-3} \text{mag}^{-1} (\times 10^{-9})$) of the RLQ, (4) error on the space density, $\sigma_\phi (\times 10^{-9})$, (5) RLF calculated using Jiang et al. (2007), (6) space density ϕ ($\text{Mpc}^{-3} \text{mag}^{-1} (\times 10^{-8})$) of the QSOs (RQ+RL), (7) indication if the bin is intersected by the limiting magnitude curve (1 = yes and 0 = no), (8) actual number of QSOs in the bin, (9) the corrected number of QSOs in the bin after applying the completeness corrections, (10) Number of QSOs in the bin limited by the radio flux limit.

Redshift (1)	M_r (2)	$\phi_{RL} (\times 10^{-9})$ (3)	$\sigma_\phi (\times 10^{-9})$ (4)	RLF (5)	$\phi (\times 10^{-8})$ (6)	Fill (7)	N_Q (8)	N_{Qcorr} (9)	N_r (10)
3.8	-26.75	3.129	1.400	3.17(± 1.60) per cent	9.870	1	5	9.43	0
3.8	-27.05	3.778	0.890	3.58(± 1.82) per cent	10.559	1	18	33.96	0
3.8	-27.35	3.242	0.744	4.04(± 2.07) per cent	8.025	0	19	35.85	1
3.8	-27.65	1.240	0.469	4.56(± 2.36) per cent	2.717	0	7	13.21	1
3.8	-27.95	1.260	0.476	5.15(± 2.69) per cent	2.447	0	7	13.21	1
3.8	-28.25	0.849	0.379	5.80(± 3.01) per cent	1.463	0	5	9.43	0
3.8	-28.55	0.679	0.339	6.53(± 3.50) per cent	1.040	0	4	7.55	0
3.8	-28.85	0.170	0.170	7.35(± 4.00) per cent	0.231	0	1	1.89	0
3.8	-29.15	0.340	0.240	8.26(± 4.58) per cent	0.411	0	2	3.77	0
3.8	-29.45	0.170	0.170	9.26(± 5.24) per cent	0.183	0	1	1.89	0
3.8	-29.75	0.170	0.170	10.39(± 6.01) per cent	0.163	0	1	1.89	0
4.2	-27.05	1.920	1.920	3.04(± 1.60) per cent	6.316	1	1	1.89	0
4.2	-27.35	0.657	0.464	3.44(± 1.81) per cent	1.910	1	2	3.77	0
4.2	-27.65	0.917	0.410	3.89(± 2.07) per cent	2.358	0	5	9.43	0
4.2	-27.95	0.550	0.318	4.39(± 2.36) per cent	1.254	0	3	5.66	0
4.2	-28.25	0.367	0.260	4.95(± 2.69) per cent	0.741	0	2	3.77	0
4.2	-28.55	0.367	0.260	5.58(± 3.07) per cent	0.658	0	2	3.77	0
4.2	-29.15	0.183	0.183	7.07(± 4.01) per cent	0.260	0	1	1.89	0
4.2	-30.05	0.183	0.183	10.02(± 6.03) per cent	0.183	0	1	1.89	0

of sources included in our sample depends on redshift. In particular, using a radio spectral index of $\alpha_r = -0.3$, at the lowest redshift of our sample, i.e. $z = 3.6$, the FIRST flux-density limit corresponds to radio luminosity $\log P_{1.4, \text{GHz}} (\text{W Hz}^{-1}) > 25.61$. For $z = 4$, it corresponds to $\log P_{1.4, \text{GHz}} (\text{W Hz}^{-1}) > 25.7$ and for $z = 4.4$ to $\log P_{1.4, \text{GHz}} (\text{W Hz}^{-1}) > 25.77$.

8.1 The space density of RLQ at $3.6 \leq z \leq 4.4$

Starting with the binned LF determined in Section 8.2, we calculate the space density of RLQ with optical luminosity $M_{1450} \lesssim -25.8$ and radio luminosity $\log P_{1.4, \text{GHz}} (\text{W Hz}^{-1}) > 25.5$, in two shells of redshift. The first shell has median $z \approx 3.8$ ($3.6 \leq z \leq 4.015$) and the second shell has median $z \approx 4.2$ ($4.015 \leq z \leq 4.415$). Integrating

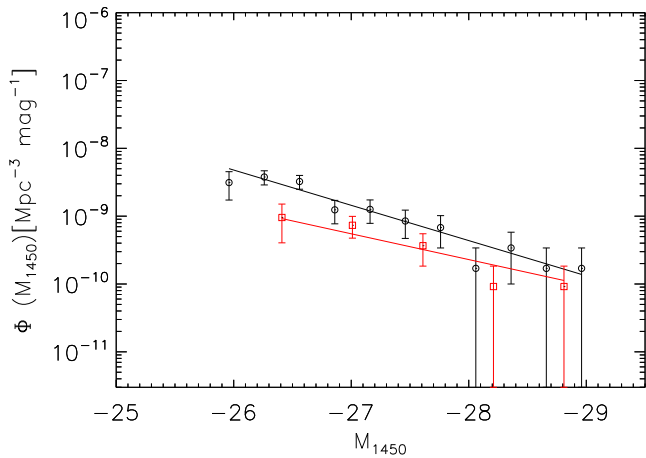


Figure 11. The LF derived from our sample of 87 RLQ with $\log_{10} P_{1.4, \text{GHz}} (\text{W Hz}^{-1}) > 25.7$. The LF for $z \sim 3.8$ is shown with black points, while red squares show the LF for $z \sim 4.2$. Black and red lines are the best-fitting slopes.

the binned LF (Table 6), the space densities of QSOs are therefore:

$$\begin{aligned} \rho(z \approx 3.8, M_{1450} < -25.8)_{\text{RL}} &= 4.51 \pm 0.61 \text{ Gpc}^{-3} \\ \rho(z \approx 4.2, M_{1450} < -25.8)_{\text{RL}} &= 1.54 \pm 0.63 \text{ Gpc}^{-3}. \end{aligned}$$

From a sample of radio QSOs obtained by cross-matching the FIRST radio survey and the Automatic Plate Measuring Facility catalogue of POSS I, Vigotti et al. (2003) measured the space density at $3.8 \leq z \leq 4.5$ of optically luminous ($M_{1450} < -26.9$) RLQ and obtained $\rho(z \approx 4.1, M_{1450} < -26.9)_{\text{RL}} = 0.99 \pm 0.28 \text{ Gpc}^{-3}$. We recalculated the space density and optical luminosities using our adopted cosmology (noted at the end of Section 1), obtaining $\rho(z \approx 4.1, M_{1450} < -27.1)_{\text{RL}} = 0.66 \pm 0.18 \text{ Gpc}^{-3}$. By integrating our binned LF in the interval $M_{1450} \lesssim -27.0$, we obtain

$$\begin{aligned} \rho(z \approx 3.8, M_{1450} < -27.0)_{\text{RL}} &= 1.09 \pm 0.24 \text{ Gpc}^{-3} \\ \rho(z \approx 4.2, M_{1450} < -27.0)_{\text{RL}} &= 0.50 \pm 0.16 \text{ Gpc}^{-3} \end{aligned}$$

in good agreement with Vigotti et al. (2003, see Fig. 12) and consistent with a linear decrease of space density with increasing redshift.

Using a sample of QSOs obtained by cross-matching FIRST and SDSS-DR6, McGreer et al. (2009) calculated a binned LF in the redshift range $3.5 \leq z \leq 4.0$. These authors used the same starting surveys as we did and a similar range of redshift, but they calculated the LF only for QSOs with radio-loudness parameter $R > 70$. The R parameter is another common criterion for distinguishing between radio-quiet and radio-loud AGN. It is defined (Kellermann et al. 1989; Stocke et al. 1992) as the rest-frame ratio of the monochromatic 6-cm (5 GHz) and 2500 Å flux densities. Generally, objects are considered to be RL for $R > 10$.

The space density calculated in McGreer et al. (2009) for $M_{1450} < -26.1$ is $\rho(z = 3.75, M_{1450} < -26.1)_{R > 70} = 1.38 \pm 0.59 \text{ Gpc}^{-3}$. The cosmology parameters used by McGreer et al. (2009) are the same that we use.

At redshift ≈ 4 , our definition of radio-loudness is very close to the common definition $R > 10$, but we needed to re-calculate the LF using a subsample of RLQ with $R > 70$ in order to compare our LF with McGreer et al. (2009). To calculate the R parameter for our sample of QSOs, we used $\alpha_\nu = -0.5$ (in agreement with McGreer et al. 2009) to transform the flux from $S_{1.4\text{GHz}}$ to $S_{5\text{GHz}}$. We follow

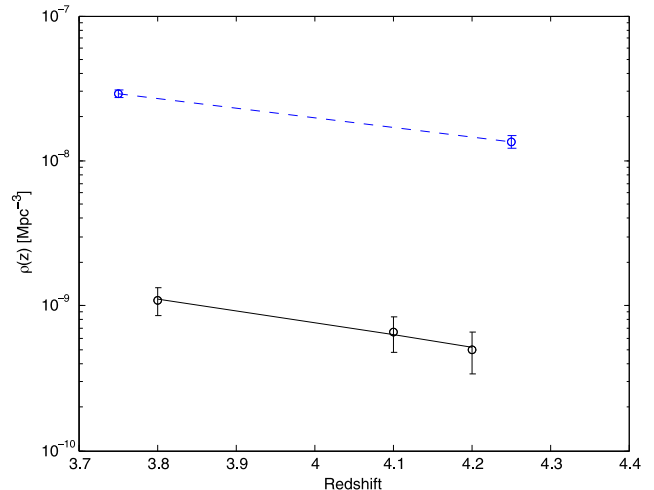


Figure 12. The black points show the integrated LF for RLQ with $M_{1450} < -27.0$. The points for $z \sim 3.8$ and 4.2 were obtained in this work, showing good agreement with the point obtained for $z \sim 4.1$ in Vigotti et al. (2003). For comparison, blue points show the space density for the entire population of QSOs and for $M_{1450} < -27.6$, as found in Richards et al. (2006). See Section 8.1.

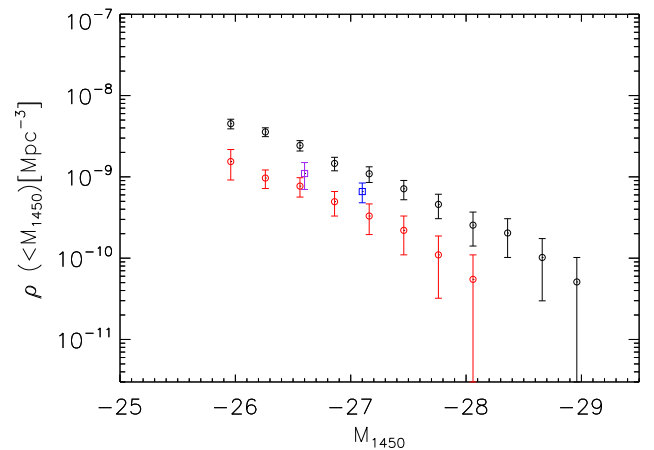


Figure 13. Cumulative LFs at $z = 3.8$ (black circles) and $z = 4.2$ (red circles). Squares represent space densities derived by Vigotti et al. (2003, blue square) and Carballo et al. (2006, purple square) at redshifts $z \sim 4.1$ and 4 , respectively.

Oke & Gunn (1983) when converting from magnitude to luminosity (2500 Å). In this way, we obtain

$$\rho(z = 3.8, M_{1450} < -26.1)_{R > 70} = 2.49 \pm 0.36 \text{ Gpc}^{-3}, \quad (14)$$

which is a factor 1.8 (2σ) higher than the value $\rho = 1.38 \pm 0.59 \text{ Gpc}^{-3}$ found by McGreer et al. (2009). This difference may in part be ascribed to the higher completeness of our NN selection, and in part to the smaller FIRST-SDSS matching radius used by McGreer et al. (2009), which will exclude some quasars.

In Fig. 13, we show the cumulative LF for the two redshift bins (i.e. $z = 3.8$ and 4.2). Each point of the cumulative function is the space density $\rho(<M_{1450})$ as a function of absolute magnitude. The two functions can be compared with previous results by Vigotti et al. (2003) and Carballo et al. (2006), at redshifts $z \sim 4.1$ and 4 , respectively. As expected, due to the evolution of space density with redshift, these last two values lie between our determinations.

8.2 Total space density of QSOs at $3.6 \leq z \leq 4.4$

From the space density of the RLQ population, we can roughly test the predictions of RLF over this range of redshift, by comparing the implied total space densities with measurements of space density from the literature.

It has long been known that between 5 and 15 per cent of all quasars are radio-loud (e.g. Kellermann et al. 1989; Urry & Padovani 1995; Ivezić et al. 2002). However, some authors conclude that the RLF does not change significantly with redshift (e.g. Goldschmidt et al. 1999; Stern et al. 2000; Cirasuolo et al. 2003) or luminosity (e.g. Bischof & Becker 1997; Stern et al. 2000; Vigotti et al. 2003), while others find that the RLF decreases with increasing redshift (e.g. Peacock, Miller & Longair 1986; Miller et al. 1990; Schneider et al. 1992; Visnovsky et al. 1992) and decreasing optical luminosity (Padovani 1993; La Franca et al. 1994); or that it evolves non-monotonically with redshift and luminosity (e.g. Hooper et al. 1995).

We therefore derive below the space density of all QSOs in two different ways: assuming constant RLF (Section 8.2.1) and using a recently determined redshift- and luminosity-dependent RLF (Jiang et al. 2007, Section 8.2.2).

8.2.1 For constant RLF

From our binned LF, we derive the space density for $M_{1450} < -26.1$ (equivalent to the limit of $M_i < -27.6$ in Richards et al. 2006) as

$$\rho(z = 3.8, M_{1450} < -26.1)_{\text{RL}} = 3.57 \pm 0.44 \text{ Gpc}^{-3}$$

$$\rho(z = 4.2, M_{1450} < -26.1)_{\text{RL}} = 1.54 \pm 0.63 \text{ Gpc}^{-3}.$$

In Vigotti et al. (2003), the RLF is assumed almost constant and is estimated as

$$\text{RLF}(M_{1450} < -26.9) = 13.3 \text{ per cent.}$$

Therefore, for the total QSO population we obtain

$$\rho(z = 3.8, M_{1450} < -26.1) = 26.8 \pm 3.3 \text{ Gpc}^{-3}$$

$$\rho(z = 4.2, M_{1450} < -26.1) = 11.6 \pm 4.7 \text{ Gpc}^{-3}$$

in good agreement with the space densities derived from Richards et al. (2006):

$$\rho(z = 3.75, M_{1450} < -26.1) = 29.0 \pm 2.0 \text{ Gpc}^{-3}$$

$$\rho(z = 4.2, M_{1450} < -26.1) = 13.6 \pm 1.3 \text{ Gpc}^{-3}.$$

8.2.2 For redshift- and luminosity-dependent RLF

Jiang et al. (2007) use a sample of more than 30 000 optically selected QSOs from the SDSS to study the evolution of the RLF as a function of redshift and luminosity. They find that the RLF of QSOs decreases with increasing redshift and decreasing luminosity, according to

$$\log \frac{\text{RLF}}{(1 - \text{RLF})} = b_o + b_z \log(1 + z) + b_M (M_{2500} + 26), \quad (15)$$

where M_{2500} is the absolute magnitude at rest frame 2500 Å. The parameters b_o , b_z and b_M depend on the value of radio-loudness and for $R > 10$; they are $b_o = -0.132 \pm 0.116$, $b_z = -2.052 \pm 0.261$, $b_M = -0.183 \pm 0.025$. M_{2500} is calculated from M_r as

$$M_{2500} = M_r + 2.5\alpha_v \log \left(\frac{2500 \text{ \AA}}{6231 \text{ \AA}} \right). \quad (16)$$

We used the Jiang et al. (2007) formula to obtain for each bin the corresponding value of the RLF (column 5 in Table 5). The RLF lies in the range 3–10 per cent, and increases with decreasing ϕ_{RL} . Applying the corresponding RLF to each bin and integrating, we obtain

$$\rho(z \approx 3.8, M_{1450} < -26.1) = 81.7 \pm 31.7 \text{ Gpc}^{-3}$$

$$\rho(z \approx 4.2, M_{1450} < -26.1) = 41.0 \pm 31.1 \text{ Gpc}^{-3}.$$

This is a factor ~ 3 higher than the results from Richards et al. (2006), but still within 2σ , due to the large errors in the LF and in the RLF. In particular, the errors on the RLF at this redshift and magnitude are ~ 50 per cent. Given that our determination of the radio-loud LF agrees reasonably well with McGreer et al. (2009) and with Vigotti et al. (2003), this discrepancy cannot be attributed solely to a possible overestimation of our LF but may also be due to a systematic underestimation of the RLF in Jiang et al. (2007). The large quoted errors invite caution when using the Jiang et al. (2007) formula to determine the fraction of radio-loud quasars at high redshifts.

8.3 The bright-end slope of the LF for RLQ

The QLF is usually well fitted by a double-power-law parametrization that takes into account the redshift (e.g. Pei 1995; Peterson 1997; Boyle et al. 2000; Croom et al. 2004; Richards et al. 2006):

$$\phi(L, z) = \frac{\phi^*/L^*}{(L/L^*(z))^{-\alpha} + (L/L^*(z))^{-\beta}}, \quad (17)$$

where α , β , ϕ^* , L^* are the faint-end slope, the bright-end slope, the normalization of the LF and the characteristic break luminosity, respectively. This model, if $\alpha > \beta$, can be approximated by

$$\phi \propto \begin{cases} L^\beta & \text{if } L \gg L^* \\ L^\alpha & \text{if } L \ll L^*. \end{cases} \quad (18)$$

As already mentioned, we calculated the LF in terms of optical luminosity in two bins of redshift. We compare our results and the best-fitting slope with those of Richards et al. (2006) for the entire population of QSOs, and with the results of McGreer et al. (2009) for RLQ with $R > 70$. The limiting magnitude of the QSOs samples used by these authors ($M_{1450} < -26.1$ for Richards et al. 2006 and McGreer et al. 2009) was considered bright enough and far from the break luminosity to approximate the LF by a single power law $\propto L^\beta$.

This kind of approximation led in recent years to a long debate about an apparent flattening of the bright-end slope for $z > 4$, after it was noticed in early high-redshift surveys (Schmidt, Schneider & Gunn 1995; Fan et al. 2001). These authors showed that the slope at $z > 4$ had a value $\beta \approx -2.5$, much shallower than the one seen at $z < 2.2$ ($\beta = -3.3$; Croom et al. 2004). This flattening was then confirmed by Richards et al. (2006) who used a large, homogeneous QSO sample from the SDSS-DR3 extending to $z = 5$. At higher redshift, the constraints are weaker as they come from small samples, but in general they do not confirm a continued flattening of the slope with increasing redshift. In fact, Willott et al. (2010), combining the Canada–France High- z quasar survey with the more luminous SDSS sample, derived the QLF from a sample of 40 QSOs at redshifts $5.74 < z < 6.42$ and found $-3.8 < \beta < -2.3$. At redshift $z \sim 6$, Jiang et al. (2008) find $\beta = -3.1 \pm 0.4$ using QSOs from SDSS Stripe 82.

Evolution of the shape of the QLF with redshift (changes in the slopes or in the location of the break luminosity) provides one of the fundamental observational constraints to the growth of SMBHs over cosmic time. Assuming that brighter AGN have more massive

black holes, the flattening of the bright end would be a remarkable indication of a downsizing of the SMBHs at high redshift. Downsizing was reported also by X-ray surveys (Ueda et al. 2003; Hasinger, Miyaji & Schmidt 2005; see also Brusa et al. 2009).

On the other hand, recent work by Shen & Kelly (2012) and McGreer et al. (2013) aims to fill the gap in the QLF between $z \sim 3.5$ and 6, with the purpose of testing the flattening of the bright-end slope at $z > 3$. Shen & Kelly (2012) constrain the LF by Bayesian modelling and using an homogeneous sample of SDSS-DR7 QSOs at $z = 0.3\text{--}5$. The results of Shen & Kelly (2012) and Richards et al. (2006) are, in general, in good agreement, finding that the curvature of the LF changes significantly beyond $z = 3$. However, Shen & Kelly (2012) suggest that the apparent flattening of the slope appears to be more related to a strong evolution of the break luminosity than a change in the bright-end slope. A similar conclusion is drawn by McGreer et al. (2013), who find no evidence for an evolution in the bright-end slope at $M_{1450} < -26$ for a sample of QSOs with $4.7 \leq z \leq 5.1$. On the other hand, McGreer et al. (2013) find evidence of strong evolution in the break luminosity, as it brightens from $M_{1450}^* \approx -25.4$ at $z = 2.5$ to $M_{1450}^* \approx -27.2$ at $z = 5$. They conclude that this evolution could flatten the bright-end slopes for surveys where the faint limit is near the break luminosity. McGreer et al. (2013) compared different models for the evolution of the QLF normalization and break luminosity. Eventually, they found a good fit of their data with recent results from the literature, using a modified version of a luminosity evolution and density evolution (LEDE) model proposed by Ross et al. (2012). In particular, the evolution of the break luminosity in this model is log-linear (up to $z \sim 5$), with a break luminosity that brightens with redshift. This modified LEDE model predicts that for $z \sim 3.8$ the break luminosity would be $M_{1450}^* \sim -26.2$ and for $z \sim 4.2$ it would be $M_{1450}^* \sim -26.4$.

If we approximate the LF by a single power law $\propto L^\beta$, we find that in the first bin of redshift, $z \sim 3.8$, our best-fitting slope is $\beta = -2.3 \pm 0.2$. As shown in Fig. 14, our best fit is in good agreement with the slope found in Richards et al. (2006, $\beta = -2.4 \pm 0.1$),

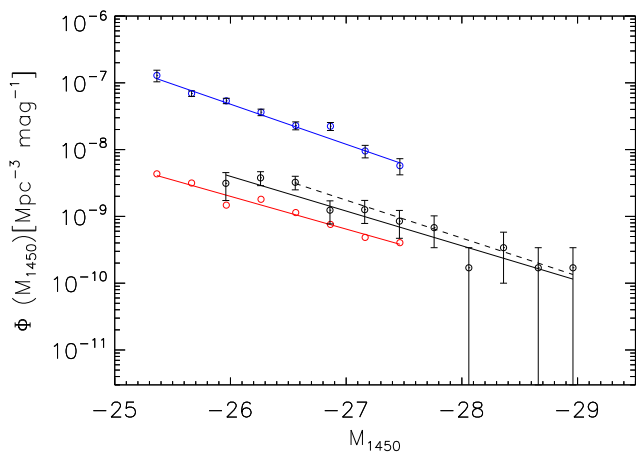


Figure 14. Black points show the LF derived for $z \sim 3.8$, for RLQ with $\log_{10} P_{1.4, \text{GHz}} (\text{W Hz}^{-1}) > 25.7$. For comparison, red points show the LF calculated by McGreer et al. (2009), for RLQ with radio-loudness $R > 70$, and blue points the LF as calculated by Richards et al. (2006) for the entire population of QSOs. Best-fitting slopes are $\beta = -2.3$ for our LF (black line); $\beta = -2.2$ for McGreer et al. (2009, red line), $\beta = -2.4$ for Richards et al. (2006, blue line). For our LF, we obtain $\beta = -2.3$ (black line) and $\beta = -2.4$ after excluding the two fainter points (dashed line). See Section 8.3.

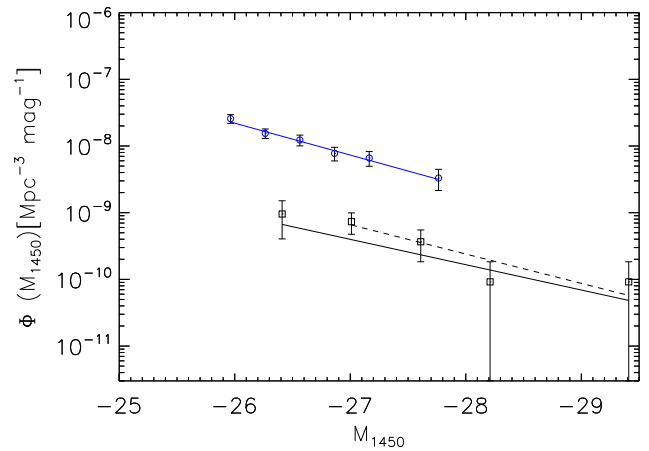


Figure 15. Black points show the LF derived for $z \sim 4.2$, for RLQ with $\log_{10} P_{1.4, \text{GHz}} (\text{W Hz}^{-1}) > 25.7$. For comparison, blue points show the LF as calculated by Richards et al. (2006) for the entire population of QSOs in the same bin of redshift. Best-fitting slope is $\beta = -2.2$ for Richards et al. (2006, blue line). For our LF, we obtain $\beta = -2.0$ (black line) and $\beta = -2.1$ after excluding the faintest point (dashed line). See section 8.3.

and with that found by McGreer et al. (2009, $\beta = -2.2 \pm 0.2$). For the RL-QLF calculated in our second bin of redshift, i.e. $z \sim 4.2$, we re-binned the LF using $\Delta M = 0.6$, in order to reduce the statistical noise. In this way, as shown in Fig. 15 the best-fitting slope is $\beta = -2.0 \pm 0.4$. This result is consistent with the result found by Richards et al. (2006) for the entire population of QSOs, i.e. $\beta = -2.2 \pm 0.1$.

Our determinations of the bright-end slope for the RL population of QSOs at $z \sim 3.8$ and 4.2 are consistent with the flattening (between these redshifts bins) of the bright-end slope found in Richards et al. (2006) for $z \geq 4$, which McGreer et al. (2013) suggest that it is due to a bias resulting from a single-fit power law in a region near the break luminosity.

As we have quasars with luminosities near or below the predicted break luminosity, we repeat the fit but excluding those points. In the first bin at redshift $z \sim 3.8$, we exclude the two fainter points. In this way, we obtain a slightly steeper best-fitting slope and a larger error: $\beta = -2.4 \pm 0.3$. This fit is shown in Fig. 14 as a dashed line. In the second bin of redshift, $z \sim 4.2$, we exclude the faintest point, obtaining again a small increase of the slope: $\beta = -2.1 \pm 0.4$. This fit is shown again as a dashed line in Fig. 15.

In light of the results from McGreer et al. (2013), our data do not strongly constrain the slope of the bright end nor the exact location of the break luminosity, especially considering the large errors of the brighter bins of the LF. Nevertheless this simple derivation is consistent with the results of McGreer et al. (2013).

In summary, our results are in good agreement with those of Richards et al. (2006) and McGreer et al. (2009). This result in itself is not trivial, because we are comparing different populations of QSOs in this range of redshift. In particular, we are comparing our results with the whole population of QSOs (by comparing with Richards et al. 2006) and with a population of RL QSOs where the radio-loudness is defined differently (being $R^* > 70$ for the RL sample of McGreer et al. 2009). We therefore have indications of a certain homogeneity of the QLF regardless of the differences in radio-loudness.

On the other hand, since we cannot constrain the bright- and the faint-end slopes, and we do not have an estimate of the break luminosity, we cannot conclude that the noted consistency of the slopes

imply also consistency of all the parameters. Any differences of the slopes, or a different value of the break luminosity, could point to different density evolution of the RL and the RQ populations. In fact, Jiang et al. (2007) express the dependence of the RLF on optical luminosity as $\approx L^{0.5}$, implying $\beta_{\text{RLQSO}} \approx \beta_{\text{QSO}} + 0.5$, which is consistent with the differences of slopes that we find between the first ($z \sim 3.8$) and the second bin ($z \sim 4.2$) of redshift. Also, Baloković et al. (2012) and Kratzer (2014) find evidence that, at high redshift, the radio-loudness distribution of quasars is not a universal function, and likely depends on redshift and/or optical luminosity. We therefore need a sample of RLQ at fainter luminosities to constrain the faint slope, and a larger survey area to extend the bright end of the LF and thus, determine the break luminosity.

9 CONCLUSIONS

We construct a sample of high-redshift RLQ $3.6 \leq z \leq 4$, and use it to measure the LF and space density of QSOs in this range of redshift. Our principal conclusions are as follows.

(i) We show (Section 3) that a simple NN can be used to select high-redshift QSOs from radio-optical surveys, with 97 per cent completeness and 60 per cent efficiency.

(ii) With the aid of the NN, we construct a sample of 87 RLQ at redshift ~ 4 . Of the various sources of incompleteness in the optical and radio surveys (Section 6), exclusion of SDSS ‘CHILD’ images is the main cause of our incompleteness relative to the SDSS selection of QSO candidates. But when applied to non-CHILD objects, our NN algorithm detects ~ 97 per cent of the high- z QSOs, while SDSS only detect ~ 85 per cent of them.

(iii) We determine the optical LF for RLQ in two redshift bins, $3.6 \leq z < 4.0$ and $4.0 \leq z \leq 4.4$ (Section 7), and measure the total comoving density of QSOs in these two redshift ranges (Fig. 12), obtaining a result consistent with that of Vigotti et al. (2003) at luminosities $M_{1450} < -27.6$. We also find good agreement between our cumulative LF (Fig. 13) and that measured by Vigotti et al. (2003) and Carballo et al. (2006), which determine the space density at intermediate redshifts.

(iv) Assuming a RLF of 13.3 per cent (Vigotti et al. 2003), we estimate the total comoving density of QSOs (Section 8.2.1). The derived density of QSOs at $z \sim 4$ is consistent with that of Richards et al. (2006). Alternatively (Section 8.2.2), using the redshift- and luminosity-dependent RLF found by Jiang et al. (2007), we measure a total comoving density of QSOs a factor 3 higher than measured by Richards et al. (2006). However, this result is significantly affected by the large error bars on the formula assumed for the RLF.

(v) We determine the slope of the LF in two bins of redshift (Section 8.3). In the lower redshift bin ($z = 3.8$), we found $\beta = -2.3 \pm 0.2$, consistent with Richards et al. (2006) and McGreer et al. (2009). In the higher redshift bin ($z = 4.2$), we find a slope $\beta = -2.0 \pm 0.4$ consistent with Richards et al. (2006). Values of the slope consistent with our determination have been interpreted as a flattening of the bright-end slope for the high- z QSOs population, but has recently been re-interpreted as the result of a strong evolution of the break luminosity for high- z QSO (McGreer et al. 2009). The consistency of our results with Richards et al. (2006) and McGreer et al. (2009) suggests a similar evolution for both radio-loud and radio-quiet populations. Our results can be also interpreted as suggestive of a flattening of the bright-end slope from $z \sim 2$ to 4, for the radio-loud population only. If confirmed, this implies an evolution of the density of SMBHs associated with RLQ, in the sense that they were more abundant at $z \sim 4$. However, to clarify the evolu-

tion of the RL population relative to that of the whole population of QSOs, more observational constraints are needed, especially at redshifts above 4. The candidate-selection approach described here is now being applied to FIRST-SDSS-UKIDSS surveys to search for QSOs at $z \gtrsim 4.5$ (Tuccillo, McMahon & González-Serrano, in preparation).

ACKNOWLEDGEMENTS

This work has been funded by the Spanish Ministerio de Ciencia e Innovación (MICINN) under project AYA2011-29517-C03-02. This paper is based on observations made with the NOT operated by the Nordic Optical Telescope Scientific Association in the Spanish Observatorio del Roque de los Muchachos on the island of La Palma. Funding for the creation and distribution of the SDSS Archive has been provided by the Alfred P. Sloan Foundation, the Participating Institutions, the National Aeronautics and Space Administration, the National Science Foundation, the US Department of Energy, the Japanese Monbukagakusho and the Max Planck Society. The SDSS website is <http://www.sdss.org/>. The Participating Institutions are the University of Chicago, Fermilab, the Institute for Advanced Study, the Japan Participation Group, the Johns Hopkins University, the Max-Planck-Institute for Astronomy (MPIA), the Max-Planck-Institute for Astrophysics (MPA), New Mexico State University, Princeton University, the United States Naval Observatory and the University of Washington. This research has made use of the NED which is operated by the Jet Propulsion Laboratory, California Institute of Technology, under contract with the National Aeronautics and Space Administration. We thank R. Carballo for the NN software and for helping to train the network and validate the selection of QSOs candidates. We acknowledge the helpful discussions with Richard G. McMahon during early stages of this work. Finally, we thank our anonymous referee for giving constructive comments, which substantially helped improving the article.

REFERENCES

- Abazajian K. N. et al., 2009, *ApJS*, 182, 543
 Avni Y., Bahcall J. N., 1980, *ApJ*, 235, 694
 Baloković M., Smolčić V., Ivezić Ž., Zamorani G., Schinnerer E., Kelly B. C., 2012, *ApJ*, 759, 30
 Becker R. H., White R. L., Helfand D. J., 1995, *ApJ*, 450, 559
 Benn C. R., Vigotti M., Pedani M., Holt J., Mack K.-H., Curran R., Sánchez S. F., 2002, *MNRAS*, 329, 221
 Bernal J., 1988, National Institute of Standards and Technology Technical Note 1252: On Constructing Delaunay Triangulations for sets Constrained by Line Segments. National Institute of Standards and Technology, Gaithersburg, MD
 Bischof O. B., Becker R. H., 1997, *AJ*, 113, 2000
 Boyle B. J., Shanks T., Croom S. M., Smith R. J., Miller L., Loaring N., Heymans C., 2000, *MNRAS*, 317, 1014
 Brusa M. et al., 2009, *ApJ*, 693, 8
 Carballo R., González-Serrano J. I., Montenegro-Montes F. M., Benn C. R., Mack K.-H., Pedani M., Vigotti M., 2006, *MNRAS*, 370, 1034
 Carballo R., González-Serrano J. I., Benn C. R., Jiménez-Luján F., 2008, *MNRAS*, 391, 369 (C08)
 Cattaneo A. et al., 2009, *Nature*, 460, 213
 Cirasuolo M., Celotti A., Magliocchetti M., Danese L., 2003, *MNRAS*, 346, 447
 Cristiani S., Vio R., 1990, *A&A*, 227, 385
 Croom S. M., Smith R. J., Boyle B. J., Shanks T., Miller L., Outram P. J., Loaring N. S., 2004, *MNRAS*, 349, 1397
 Croom S. M. et al., 2009, *MNRAS*, 399, 1755
 de Vries W. H., Becker R. H., White R. L., 2006, *AJ*, 131, 666

- Dole H. et al., 2006, *A&A*, 451, 417
 Ellis R. S., Colless M., Broadhurst T., Heyl J., Glazebrook K., 1996, *MNRAS*, 280, 235
 Elvis M. et al., 1994, *ApJS*, 95, 1
 Fabian A. C., 2012, *ARA&A*, 50, 255
 Fan X. et al., 2001, *AJ*, 121, 54
 Felten J. E., 1976, *ApJ*, 207, 700
 Giallongo E., Menci N., Fiore F., Castellano M., Fontana A., Grazian A., Pentericci L., 2012, *ApJ*, 755, 124
 Goldschmidt P., Kukula M. J., Miller L., Dunlop J. S., 1999, *ApJ*, 511, 612
 Gregg M. D., Becker R. H., White R. L., Helfand D. J., McMahon R. G., Hook I. M., 1996, *AJ*, 112, 407
 Hagan M., Menhaj M.-B., 1994, *IEEE Trans. Neural Netw.*, 5, 989
 Hasinger G., Miyaji T., Schmidt M., 2005, *A&A*, 441, 417
 Hazard C., Mackey M. B., Shimmins A. J., 1963, *Nature*, 197, 1037
 Hickox R. C., Markevitch M., 2006, *ApJ*, 645, 95
 Hogg D. W., Baldry I. K., Blanton M. R., Eisenstein D. J., 2002, [arXiv:astro-ph/0210.394](https://arxiv.org/abs/astro-ph/0210.394)
 Hooper E. J., Impey C. D., Foltz C. B., Hewett P. C., 1995, *ApJ*, 445, 62
 Humason M. L., Mayall N. U., Sandage A. R., 1956, *AJ*, 61, 97
 Ivezić Ž. et al., 2002, *AJ*, 124, 2364
 Jiang L., Fan X., Ivezić Ž., Richards G. T., Schneider D. P., Strauss M. A., Kelly B. C., 2007, *ApJ*, 656, 680
 Jiang L. et al., 2008, *AJ*, 135, 1057
 Kellermann K. I., Sramek R., Schmidt M., Shaffer D. B., Green R., 1989, *AJ*, 98, 1195
 Kratzer R. M., 2014, PhD thesis, Drexel Univ.
 La Franca F., Gregorini L., Cristiani S., de Ruiter H., Owen F., 1994, *AJ*, 108, 1548
 Maccacaro T., della Ceca R., Gioia I. M., Morris S. L., Stocke J. T., Wolter A., 1991, *ApJ*, 374, 117
 McGreer I. D., Helfand D. J., White R. L., 2009, *AJ*, 138, 1925
 McGreer I. D. et al., 2013, *ApJ*, 768, 105
 Marshall H. L., Tananbaum H., Avni Y., Zamorani G., 1983, *ApJ*, 269, 35
 Miller L., Peacock J. A., Mead A. R. G., 1990, *MNRAS*, 244, 207
 Miyaji T., Hasinger G., Schmidt M., 2001, *A&A*, 369, 49
 Netzer H., Trakhtenbrot B., 2007, *ApJ*, 654, 754
 Oke J. B., Gunn J. E., 1983, *ApJ*, 266, 713
 Padovani P., 1993, *MNRAS*, 263, 461
 Page M. J., Carrera F. J., 2000, *MNRAS*, 311, 433
 Peacock J. A., Miller L., Longair M. S., 1986, *MNRAS*, 218, 265
 Pei Y. C., 1995, *ApJ*, 438, 623
 Peterson B. M., 1997, *An Introduction to Active Galactic Nuclei*. Cambridge: Cambridge Univ. Press
 Prandoni I., Gregorini L., Parma P., de Ruiter H. R., Vettolani G., Wieringa M. H., Ekers R. D., 2001, *A&A*, 365, 392
 Richards G. T. et al., 2002, *AJ*, 123, 2945
 Richards G. T. et al., 2006, *AJ*, 131, 2766
 Ross N. P. et al., 2012, *ApJS*, 199, 3
 Samantaray A., Khare P., 2000, *AJ*, 21, 19
 Schlegel D. J., Finkbeiner D. P., Davis M., 1998, *ApJ*, 500, 525
 Schmidt M., 1963, *Nature*, 197, 1040
 Schmidt M., 1968, *ApJ*, 151, 393
 Schmidt M., Schneider D. P., Gunn J. E., 1995, *AJ*, 110, 68
 Schneider D. P., van Gorkom J. H., Schmidt M., Gunn J. E., 1992, *AJ*, 103, 1451
 Schneider D. P. et al., 2002, *AJ*, 123, 567
 Schneider D. P. et al., 2005, *AJ*, 130, 367
 Schneider D. P. et al., 2010, *AJ*, 139, 2360
 Shankar F., Crocce M., Miralda-Escudé J., Fosalba P., Weinberg D. H., 2010, *ApJ*, 718, 231
 Shen Y., Kelly B. C., 2012, *ApJ*, 746, 169
 Stern D., Djorgovski S. G., Perley R. A., de Carvalho R. R., Wall J. V., 2000, *AJ*, 119, 1526
 Stocke J. T., Morris S. L., Weymann R. J., Foltz C. B., 1992, *ApJ*, 396, 487
 Ueda Y., Akiyama M., Ohta K., Miyaji T., 2003, *ApJ*, 598, 886
 Urry C. M., Padovani P., 1995, *PASP*, 107, 803
 Vanden Berk D. E. et al., 2001, *AJ*, 122, 549
 Vanden Berk D. E. et al., 2005, *AJ*, 129, 2047
 Vigotti M., Carballo R., Benn C. R., De Zotti G., Fanti R., Gonzalez Serrano J. I., Mack K.-H., Holt J., 2003, *ApJ*, 591, 43
 Visnovsky K. L., Impey C. D., Foltz C. B., Hewett P. C., Weymann R. J., Morris S. L., 1992, *ApJ*, 391, 560
 Volonteri M., Haardt F., Madau P., 2003, *ApJ*, 582, 559
 Willott C. J. et al., 2010, *AJ*, 139, 906
 Wisotzki L., 2000, *A&A*, 353, 861
 York D. G. et al., 2000, *AJ*, 120, 1579

SUPPORTING INFORMATION

Additional Supporting Information may be found in the online version of this article:

Table 5. Computed K -correction in r . (<http://mnras.oxfordjournals.org/lookup/suppl/doi:10.1093/mnras/stv472/-/DC1>).

Please note: Oxford University Press is not responsible for the content or functionality of any supporting materials supplied by the authors. Any queries (other than missing material) should be directed to the corresponding author for the article.

This paper has been typeset from a $\text{\TeX}/\text{\LaTeX}$ file prepared by the author.